HHS Public Access

Author manuscript

Nat Neurosci. Author manuscript; available in PMC 2015 July 01.

Published in final edited form as:

Nat Neurosci. 2015 January ; 18(1): 75–86. doi:10.1038/nn.3892.

Cell-specific STORM superresolution imaging reveals nanoscale organization of cannabinoid signaling

Barna Dudok[#1,2], **László Barna**[#1], **Marco Ledri**[#1], **Szilárd I. Szabó**[1], **Eszter Szabadits**[1], **Balázs Pintér**[1], **Stephen G. Woodhams**[1], **Christopher M. Henstridge**[1], **Gyula Y. Balla**[1,2], **Rita Nyilas**[1], **Csaba Varga**[3], **Sang-Hun Lee**[3], **Máté Matolcsi**[4], **Judit Cervenak**[5], **Imre Kacskovics**[5,6], **Masahiko Watanabe**[7], **Claudia Sagheddu**[8], **Miriam Melis**[8], **Marco Pistis**[8,9], **Ivan Soltesz**[3], and **István Katona**[#,1]

[1]Momentum Laboratory of Molecular Neurobiology, Institute of Experimental Medicine, Hungarian Academy of Sciences, Budapest, Hungary

[2]School of Ph.D. Studies, Semmelweis University, Budapest, Hungar

[3]Department of Anatomy and Neurobiology, University of California, Irvine, USA

[4]Alfred Renyi Institute of Mathematics, Hungarian Academy of Sciences, Budapest, Hungary

[5]ImmunoGenes Kft, Budakeszi, Hungary

[6]Department of Immunology, Eötvös Loránd University Budapest, Hungary

[7]Department of Anatomy, Hokkaido University School of Medicine, Sapporo, Japan

[8]Department of Biomedical Sciences, University of Cagliari, Cittadella Universitaria di Monserrato, Italy

[9]CNR Neuroscience Institute, Cagliari, Italy

[#] These authors contributed equally to this work.

Abstract

[#]Corresponding author: István Katona, PhD, Institute of Experimental Medicine, Hungarian Academy of Sciences, Szigony u. 43, Budapest, Hungary, H-1083, Phone: +36-1-210-9982, katona@koki.hu.

CONFLICT OF INTEREST

J. Cervenak is scientific researcher; I. Kacskovics is scientific co-founder of ImmunoGenes Ltd., a company specialized in the generation of FcRn transgenic animals for the production of polyclonal and monoclonal antibodies. The other authors declare no competing financial interests.

AUTHOR CONTRIBUTIONS

B.D. and L.B. designed and performed STORM experiments and corresponding analytical tools, analyzed data, prepared the figures and wrote the manuscript. M.L. carried out patch-clamp electrophysiological recordings, cell reconstructions, STORM imaging and data analysis. S.I.S. conducted and analyzed *in vitro* electrophysiological measurements as well as participated in STORM imaging and data analysis. E.S., B.P, S.G.W. and R.N. developed immunostaining, tissue processing and antibody labeling procedures for STORM imaging and contributed to data acquisition and analysis. C.M.H. performed cell culture and electron microscopy experiments and data analysis. G.Y.B., J.C., I.Kacskovics, and M.W. developed and validated antibodies. C.V. performed in vivo electrophysiology. S-H.L. carried out *in vitro* electrophysiological recordings. M.Matolcsi developed mathematical analysis tools. C.S, M.Melis and M.P. designed and performed the chronic drug administration experiment. I.S. designed and supervised *in vitro* and *in vivo* electrophysiological experiments and contributed to manuscript editing. I.Katona conceived and supervised the project, performed *in vitro* electrophysiological recordings, and wrote the manuscript.

A major challenge in neuroscience is to determine the nanoscale position and quantity of signaling molecules in a cell-type-, and subcellular compartment-specific manner. We therefore developed a novel approach combining cell-specific physiological and anatomical characterization with superresolution imaging, and studied the molecular and structural parameters shaping the physiological properties of synaptic endocannabinoid signaling in the mouse hippocampus. We found that axon terminals of perisomatically-projecting GABAergic interneurons possess increased CB_1 receptor number, active-zone complexity, and receptor/effector ratio compared to dendritically-projecting interneurons, in agreement with higher efficiency of cannabinoid signaling at somatic versus dendritic synapses. Furthermore, chronic Δ^9-tetrahydrocannabinol administration, which reduces cannabinoid efficacy on GABA release, evoked dramatic CB_1-downregulation in a dose-dependent manner. Full receptor recovery required several weeks after cessation of Δ^9-tetrahydrocannabinol treatment. These findings demonstrate that cell-type-specific nanoscale analysis of endogenous protein distribution is possible in brain circuits, and identify novel molecular properties controlling endocannabinoid signaling and cannabis-induced cognitive dysfunction.

Mechanistic understanding of biological processes requires integrated analysis of structural and functional parameters together with their underlying molecular dynamics. However, this is uniquely difficult to achieve in the brain due to its cellular and molecular diversity[1-4]. Cortical circuits are composed of many types of excitatory principal cells and inhibitory interneurons[1], which play distinct computational roles in network activity[4]. To sculpt their synaptic interactions, autonomous cell-type-, and synapse-specific processes dynamically optimize the position and density of hundreds of signaling molecules[3,5]. Despite considerable efforts[2], cell-type-specific nanoscale imaging of synaptic proteins in combination with physiological and morphological investigations has remained technically challenging in intact brain circuits. As a result, our knowledge of the quantitative molecular properties dictating various structural and functional parameters of synaptic transmission is still incomplete.

Retrograde endocannabinoid signaling mediates many forms of synaptic plasticity via CB_1 cannabinoid receptor activation[6,7]. Although CB_1 is one of the most widespread presynaptic regulators of neurotransmitter release in the brain[8], the principles characterizing its cell-type-specific subcellular distribution and density have remained elusive. The *locus classicus* for the demonstration of presynaptic CB_1 receptors[9] and their involvement in retrograde signaling is the hippocampal GABAergic synapse[10,11]. Two major forms of CB_1-containing GABAergic interneurons are specialized to target either the perisomatic or dendritic regions of principal cells[1,12,13]. Importantly, perisomatic and dendritic inhibition have markedly different physiological functions[14]. In line with this functional division of labor, endocannabinoid-mediated synaptic plasticity is remarkably stronger at synapses derived from perisomatically-projecting CB_1-positive interneurons compared to synapses belonging to dendritically-projecting CB_1-expressing cells[15]. Moreover, low doses of cannabinoids inhibit GABA release from perisomatic interneurons, but not from dendritic cells[15]. While these findings imply that some of the molecular properties underlying CB_1-dependent synaptic regulation must be different at specific circuit locations, our understanding of the

molecular parameters determining the strength of retrograde synaptic transmission is still very limited.

Cannabinoid signaling is also altered in a cell-type-specific manner under pathophysiological conditions. For example, exposure to Δ^9-tetrahydrocannabinol (THC), the psychoactive cannabis constituent strongly diminishes cannabinoid signaling efficacy on GABA release, but not on glutamate release[16], emphasizing the cell-type-specific nature of pathological alterations involving CB_1 receptors. THC has been suggested to cause cognitive deficits primarily by activating cannabinoid receptors on GABAergic boutons[17,18], however, the molecular mechanisms underlying THC-induced functional tolerance and perturbed cannabinoid signaling remain poorly understood.

The above results highlight the need for a cell-type-specific method to enable high-yield, high-resolution analysis of protein distribution in brain circuits. The recent advent of superresolution microscopy has introduced potential alternatives for molecular imaging[19]. Here, we introduce a rapid and versatile approach based on STochastic Optical Reconstruction Microscopy (STORM)[20] for cell-type-specific superresolution imaging. As a proof of principle, we demonstrate the power of the new methodology by applying it to the study of the molecular and structural heterogeneity and pathophysiological plasticity of synaptic endocannabinoid signaling. The results uncover cell-type-specific molecular properties of cannabinoid-sensitive GABAergic axon terminals at nanoscale resolution, and elucidate functional tolerance-related changes in CB_1 distribution after chronic THC exposure, providing insights into the domain-specific efficiency of endocannabinoid signaling and the mechanisms underlying cognitive impacts of cannabis use.

RESULTS

STORM superresolution imaging of CB_1 cannabinoid receptors

We first developed an approach to combine confocal/STORM imaging and tested whether it reliably determines CB_1 receptor position in a cellular membrane environment using an EGFP-tagged CB_1-construct (Supplementary Fig. 1a; Online Methods). Acquiring correlated confocal and 3D-STORM images revealed that both the intrinsic EGFP fluorescence signal and the STORM signal representing immunostaining for CB_1 were concentrated in the plasma membrane of HEK cells (Supplementary Fig. 1b,c). However, while the outline of the membrane was not resolved in the confocal image due to light diffraction, sub-diffraction-limit STORM imaging visualized sharp plasma membrane contours (Supplementary Fig. 1,e,f). Importantly, the Number of CB_1 Localization Points (CB_1 NLPs) exhibited very tight, positive correlation with the corresponding EGFP fluorescence intensity (Supplementary Fig. 1d), emphasizing the quantitative potential of 3D-STORM imaging to compare receptor distribution between distinct anatomical profiles or to measure molecular changes within the same profile.

To enable high-throughput, quantitative, cell-type-specific nanoscale analysis of endogenous protein distribution in brain circuits, we then designed widely applicable tissue processing and immunolabeling protocols for 3D-STORM microscopy (Online Methods). Presynaptic CB_1 receptor distribution was examined in 7051 individual GABAergic axon terminals at an

imaging speed of 2 minutes, and with a measured fluorophore localization precision of 6 nm in the lateral and 41 nm in the axial dimensions, as determined from the same images obtained at ~5 μm depth (Supplementary Fig. 2). Thus, this rapid and efficient workflow reveals protein distribution with high precision, but allows a sample size that is beyond the reach of immunogold electron microscopy. In hippocampal sections derived from $CB_1^{+/+}$ mice, STORM imaging uncovered high CB_1 receptor density on cholecystokinin (CCK)-containing GABAergic axon terminals forming typical basket-like arrays around the CB_1-immunonegative somata of CA1 pyramidal neurons (Fig. 1a-c). Notably, adjacent CB_1/CCK-positive boutons were often difficult to resolve in diffraction-limited immunofluorescence images (Fig. 1d,e), whereas STORM imaging reliably resolved the same structures (Fig. 1f). In contrast, the absence of localization points in CCK-positive boutons derived from littermate $CB_1^{-/-}$ mice validated antibody specificity and the staining and imaging protocols (Fig. 1g-i). Taken together, these experiments demonstrate that nanoscale molecular investigations in brain circuits are feasible with high-yield, strong sensitivity and good specificity by using 3D-STORM imaging.

Cell- and synapse-specific nanoscale molecular imaging

The precise subcellular localization and density of synaptic proteins vary in relation to physiological and pathophysiological processes in a cell-type-specific manner[3]. STORM imaging provides a list of 3D coordinates of target protein localizations, but does not readily position these coordinates in the cell-type-specific context required for functional interpretation in light of the immense cellular complexity of brain circuits. Thus, we developed an approach combining patch-clamp electrophysiology, confocal imaging of biocytin-filled neurons and STORM superresolution imaging of target proteins overlaid on the identified subcellular structure (Online Methods). As a major advantage, this combination of methods offers unique opportunity to collect physiological and morphological information from the same neuron, providing quantitative data on multiple target protein distributions in its identified axon terminals within one week (Fig. 2).

Despite its prominent role in neurotransmitter release regulation[8], the cell-type-specific principles establishing CB_1 number and location on a given axon terminal type remain unknown. To address this issue, we first performed whole-cell patch-clamp recordings from multipolar neurons located in CA1 stratum radiatum in acute slice preparations. Most neurons exhibited accommodating regular-spiking firing pattern (Fig. 2a,g), a physiological signature of CB_1/CCK-expressing interneurons[15]. These cells were filled with biocytin during recording and then imaged and reconstructed by confocal microscopy and Neurolucida (Fig. 2b,h). To classify these interneurons quantitatively, we developed a novel bouton distribution index (BDI) based on descriptive statistics of the extent of layer-specific varicosity concentration ($n = 997 \pm 58$ boutons/cell; $n = 79$ cells; Online Methods). Importantly, BDI unequivocally discriminated these cells either as perisomatic interneurons (BDI > 1), such as basket cells[13,21] which synapse on the somata and proximal dendrites of principal cells in stratum pyramidale (Fig. 2b,c); or as dendritic interneurons (BDI < 0.5), such as Schaffer collateral-associated cells[13,21], which preferentially target the distal dendritic shafts of pyramidal neurons in strata radiatum and oriens (Fig. 2h,i). These perisomatic and dendritic interneurons also differed in certain physiological characteristics

such as spike width, afterhyperpolarization amplitude and accommodation ratio (Supplementary Fig. 3; Supplementary Table).

Subsequent CB_1-immunostaining for STORM imaging was performed on 20 μm-thick free-floating sections prepared from the acute slice. Identified axon terminals of perisomatic or dendritic interneurons were imaged by confocal microscopy (n = 46±2 boutons/cell; Fig. 2d,j). CB_1 localization points within a given varicosity were then visualized by 3D-STORM microscopy overlaid on the corresponding confocal image (Fig. 2e,f,k,l). We conducted several control experiments, which ruled out possible distorting effects of differences in tissue handling (Supplementary Fig. 4a), in antibodies (Supplementary Fig. 4b), and in whole-cell manipulations (Supplementary Fig. 4c,d). Collectively, these experiments illustrate that cell-type-specific STORM imaging can readily be performed in brain circuits and showcase the combination of physiological and anatomical analyses with nanoscale molecular imaging in CB_1-positive perisomatic and dendritic interneurons.

CB_1 abundance scales with bouton size in GABAergic cells

Because cannabinoid signaling is more effective at perisomatic GABAergic synapses compared to dendritic connections[15], we next aimed to determine which molecular and structural parameters may contribute to this cell-type-specific physiological difference. Axon terminals of perisomatic and dendritic interneurons had similar shapes (Supplementary Fig. 5), but the former were significantly larger (Fig. 3a,b). Likewise, perisomatic terminals contained 39% more CB_1 receptors than dendritic boutons (Fig. 3c). This observation obtained at the cell-type-level raised the possibility that these two parameters are closely related even at the individual bouton level. Indeed, both the perimeter and the area were significantly correlated with CB_1 NLPs in both cell types ($p<0.001$; Fig. 3d), implying that bouton size is a major factor that predicts CB_1 receptor number on a given axon terminal.

The cell-type-specific difference in CB_1 abundance may influence cannabinoid signaling efficacy, but it is unlikely to be the sole explanation for the higher efficacy at perisomatic synapses, since neither overall CB_1 density (Fig. 3e,f), nor local CB_1 density within 200 nm-sized surface nanodomains exhibited significant cell-type-specific differences (Supplementary Fig. 6a). Additional analyses demonstrated that CB_1 labeling density on interneuron terminals fell within the dynamic range of the measurement (Supplementary Fig. 6a-c), and the imaging conditions resulted in reliable CB_1 distribution maps (Supplementary Fig. 6d-f). Moreover, independent experiments using CB_1-immunogold labeling and electron microscopy revealed that randomly selected CB_1-positive perisomatic terminals were larger and had significantly more CB_1 receptors than dendritic boutons, but CB_1 density was not different (Supplementary Fig. 7). The distribution of normalized data obtained by 3D-STORM and electron microscopy did not differ (n = 94 and 200 boutons, respectively, Kolmogorov-Smirnov test, $p > 0.1$), corroborating that when sampling the same bouton population, the two approaches generate comparable information. On the other hand, CB_1 NLP in STORM imaging was 2.5-5-fold greater than CB_1-immunogold particle number (taking section thickness into account), offering an additional advantage for quantitative investigation of subtle molecular changes in protein quantity.

The electron microscopic analysis also showed that the vast majority of CB_1 receptors were integrated into the plasma membrane (Supplementary Fig. 7a,b; 88±1% and 85±1% of gold particles in perisomatic and dendritic boutons, respectively). Thus, the perimeter value determined from a 2D-convex hull fitted on CB_1 localization data is expected to give good estimation of bouton size (Fig. 3b). However, CB_1 distribution densely covers the entire bouton surface, whereas several other presynaptic proteins are only sparsely distributed. Thus, their visualization may not optimally support correlative morphological and molecular investigations with nanoscale precision. To circumvent this obstacle, we exploited the fact that biocytin fills out the cytoplasmic space and performed 3D-STORM imaging of the streptavidin-labeled biocytin-staining in interneuron boutons (Fig. 3g,h,j,k). Importantly, 2D-convex hull fitting onto biocytin LPs allowed bouton size measurements and confirmed that axon terminals derived from perisomatically-projecting interneurons are significantly larger than those originating from dendritic interneurons (Fig. 3m). Finally, the 3D coordinates of biocytin LPs were illustrated using Visual Molecular Dynamics, and a 3D convex hull was fitted onto the biocytin LPs. This geometric approach generated a polyhedron representation of the bouton volume and facilitated intuitive evaluation of the acquired images (Fig. 3i,l). When dual-channel directSTORM imaging was performed on biocytin-filled interneuron terminals by combining Alexa647-CB_1-immunostaining with Alexa488-streptavidin staining (Fig. 3n), the 3D-convex hulls fitted onto the localization points from either channel also visualized similar bouton surfaces (Fig. 3o). Importantly, this configuration also enables cell-type-specific nanoscale distribution analysis of less densely expressed receptors.

Uniform CB_1 receptor distribution on GABAergic boutons

Postsynaptic neurotransmitter receptors are concentrated within highly organized nanodomains[22-24], but it is not known whether such topological restrictions also characterize presynaptic neuromodulator receptor distributions. Interneuron-type-specific coupling distances between voltage-gated calcium channels (VGCCs) and the calcium sensor for vesicle release critically determine release properties[25]. A cell-type-specific CB_1 nanodomain organization resulting in distinct coupling distances to their effectors, the N-type VGCCs[26], would also offer a potential explanation for the physiological differences in cannabinoid signaling. Therefore, we took advantage of another aspect of STORM microscopy, namely, its ability to perform nanodomain-specific distribution analysis of multiple target proteins within the same sample[27].

Bassoon is a presynaptic cytomatrix protein and a constituent of the release machinery with an essential function in organizing VGCC distribution within the active zone[28]. We first asked whether 3D-STORM imaging reliably visualizes bassoon in the active zone in CB_1-containing perisomatic and dendritic axon terminals. CB_1-positive varicosities impinging on the somatodendritic surface of biocytin-labeled postsynaptic CA1 pyramidal neurons were identified by confocal microscopy (Fig. 4a,b,d,e). Double 3D-STORM imaging of CB_1-positive terminals consistently revealed intraterminal bassoon accumulation facing the postsynaptic pyramidal neuron (Fig. 4c,f), visualizing the position of the synaptic active zone.

To decipher the nanoscale distribution of CB_1 receptors in relation to the active zone in a cell-type-specific manner, we next acquired bassoon and CB_1 localization coordinates in identified axon terminals of individually labeled perisomatic or dendritic GABAergic interneurons (Fig. 4g,h,i,j; Supplementary Fig. 8a). In contrast to the nanodomain-restricted accumulation of postsynaptic ionotropic receptors[22-24], presynaptic CB_1 receptors showed a uniform distribution at the nanoscale level. The mean Euclidean distance from the bassoon localization points was not different between measured and randomized CB_1 distributions (n = 452–452 boutons, Mann-Whitney U test, $p = 0.55$), and there was no significant difference between interneuron types (Fig. 4k,m,o).

However, G protein-coupled receptors, such as CB_1, inhibit VGCCs via βγ subunits in a plasma membrane-delimited manner[29] indicating that molecular distance measurements on the membrane surface may lead to more functionally relevant information. To this end, the plasma membrane contour was approximated by fitting a 3D-convex hull onto the CB_1 localization points. We first measured the distance of localization points from the polyhedron surface and estimated the ratio between membrane-associated localization points and those that may represent intracellular (e.g. internalized) receptors (Supplementary Fig. 8b,c; Online Methods). In good agreement with our electron microscopy data, the majority of CB_1 was associated with the convex hull-approximated plasmalemma in both interneuron types (79±1% and 81±1%, n = 280 and 141 perisomatic and dendritic axon terminals, respectively). To make molecular distance measurements possible on the polyhedron surface, we next developed an approximative mathematical algorithm (Supplementary Fig. 8d; Online Methods). In selected boutons containing a single cluster of bassoon localization points, a second convex hull was fitted onto this bassoon cluster. Because bassoon is not an integral membrane protein, points on this second hull were then projected onto the CB_1 polyhedron surface. The shortest route between each CB_1 localization point and the nearest projected bassoon point along the polyhedron surface was then calculated (Fig. 4k,n). In accordance with the Euclidean distance measurements, there was no difference in CB_1 distances from the active zone between perisomatic and dendritic axon terminals (Fig. 4o). We also determined the local density of CB_1 receptors on the polyhedron surface in relation to the active zone (validated by simulation of enriched receptor distributions; Supplementary Fig. 9), which also revealed uniform CB_1 density distribution across the bouton surface and gave similar results for the two cell types (Fig. 4p). Taken together, these measurements introduced novel tools, which are easily applicable to any single-molecule localization-based microscopy data to determine molecular distances on the surface of identified subcellular compartments. Moreover, in contrast to the clustered organization of postsynaptic ionotropic receptors[22-24], these measurements unveiled a uniform distribution of presynaptic CB_1 receptors on both types of GABAergic axon terminals. Thus, the differential cannabinoid sensitivity of perisomatic and dendritic interneurons is unlikely to be explained by distinct nanoscale targeting of CB_1 receptors.

Finally, we investigated whether these data obtained in acute hippocampal slice preparations represent the natural *in vivo* state (Supplementary Fig. 10). In awake mice, we recorded the firing properties of an individual GABAergic interneuron in juxtacellular configuration, in relation to local field potentials during rhythmic brain activity (Supplementary Fig. 10a).

Concurrent biocytin labeling enabled its *post hoc* anatomical characterization and classification as a dendritic interneuron (Supplementary Fig. 10b,c). Subsequent combined confocal/STORM imaging uncovered dense CB_1 receptor labeling with high localization precision on all investigated axon terminals (n = 129; Supplementary Fig. 10d-f). Importantly, normalized CB_1 NLP distributions were similar in hippocampal GABAergic interneurons filled under *in vitro* or *in vivo* conditions (Supplementary Fig. 10g). Moreover, CB_1 surface distribution was also similar under both conditions (Supplementary Fig. 10h). Finally, CB_1 quantity on individual boutons was in positive linear correlation ($p < 0.001$) with the size of the axon terminals (Supplementary Fig. 10i). These measurements highlight the feasibility and power of the cell-type-specific methodology for an integrated analysis of *in vivo* physiological, anatomical and molecular parameters in intact brain circuits and validate our *in vitro* findings.

Different nanoscale structure of interneuron active zones

The two observations that CB_1 receptor density and nanoscale distribution pattern are similar on interneuron boutons imply that other molecular parameters account for cell-type-specific cannabinoid signaling efficacy on GABA release probability. At central synapses, active zone size tightly correlates with VGCC abundance and transmitter release probability[30]. The copy numbers of protein components in the active zone, including the quantity of bassoon and VGCC subunits, also correlate closely[31]. Thus, we hypothesized that cannabinoid effects on neurotransmitter release may be influenced by the quantitative relationship between CB_1 receptors and their nearby molecular effectors. To address this issue, we next gained insights into the organizational properties of the presynaptic release machinery of the two cannabinoid-sensitive GABAergic bouton types.

In contrast to the homogeneous CB_1 distribution on bouton surface, cell-type-specific 3D-STORM imaging of single bassoon labeling revealed clustered bassoon organization within both interneuron terminal types (Fig. 5a,b,d,e). To quantitatively evaluate clustering, we performed density-based analysis of the localization points (Fig. 5f; Online Methods). Considering the larger size and higher CB_1 numbers of perisomatic terminals, surprisingly, bassoon NLPs within these clusters were similar in the two interneuron bouton types (Fig. 5g,h). When CB_1 numbers were normalized to bassoon numbers, the resulting cell-type-specific CB_1/bassoon molecular ratio showed that perisomatic interneuron terminals have on average 49% more CB_1 receptors than those of dendritic interneurons. Given that bassoon and VGCC numbers in release machineries correlate[31], this proportional difference in receptor/effector ratio is likely to contribute to cell-type-specific cannabinoid sensitivity.

Some CB_1 receptors on bouton surface may not be able to directly regulate the release machinery due to their distant location from the active zone. Therefore, we further exploited the improved localization precision of STORM imaging to focus our analysis on CB_1 receptors located in the vicinity of bassoon clusters. Interestingly, perisomatic axon terminals contained more bassoon clusters than boutons derived from dendritic interneurons (Fig. 5i5i), but individual bassoon clusters had 26% less bassoon LPs (Fig. 5j). Furthermore, regardless of the distance from bassoon clusters, significantly more CB_1 LPs were observed in perisomatic boutons compared to their dendritic counterparts. For example, 46% more

CB_1 LPs were found within the first 100 nm bin (which includes the ~80 nm distance of bassoon from the bouton surface[27]) in perisomatic terminals (Fig. 5k). These observations are consistent with the more fragmented bassoon cluster architecture found in perisomatic boutons and the uniform CB_1 nanoscale distribution. Together with the reduced bassoon number in individual clusters, these findings indicate that a higher receptor/effector ratio in the release machinery-containing nanodomain may facilitate more efficient coupling between CB_1 and its nearby molecular effectors in perisomatic axon terminals.

The differences in the molecular parameters observed at the cell type level raise the question of which parameters are instrumental at the individual bouton level. Considering that perisomatic terminals are larger and CB_1 quantity correlates with bouton size in both interneuron types, it is plausible that some of the cell-type-specific differences are emergent consequences of distinct axon terminal sizes. Therefore, we selected perisomatic and dendritic bouton samples with identical size distributions at random (n = 200–200; Fig. 5l). Notably, CB_1 NLPs were identical between axon terminals of perisomatically- and dendritically-targeting interneurons, however, dendritic boutons contained significantly more bassoon LPs than perisomatic terminals of the same size (Fig. 5m). As a consequence, the CB_1/bassoon ratio was 27% higher in perisomatic boutons. Additionally, while the number of bassoon clusters did not differ between cell types (Fig. 5n), bassoon NLPs in individual clusters were 33% higher in dendritic boutons (Fig 5o). In accordance with having the same total number and a homogeneous distribution of CB_1 in the identically sized boutons, CB_1 NLPs were identical within any given distance from bassoon clusters (Fig. 5p). These findings indicate that similar numbers of adjacent CB_1 receptors need to control more release machineries in dendritic boutons, when comparing boutons of the same size. In conclusion, the cell-type-specific differences in receptor/effector ratio and nanoscale distance derives from distinct bassoon quantity in individual bassoon clusters and emerges from the larger number of uniformly distributed CB_1 receptors on bigger perisomatic axon terminals.

Chronic THC treatment evokes robust CB_1-downregulation

To test that CB_1 receptor number and nanoscale position are two important parameters influencing the impact of cannabinoid signaling on GABA release, we performed chronic THC treatment. Such treatment causes strong reduction in cannabinoid efficacy on GABAergic transmission[16], but the underlying molecular mechanisms of functional tolerance remain unknown. We therefore investigated the effects of repeated THC exposure on CB_1 number and distribution within identified axon terminals of perisomatic GABAergic interneurons. Chronic THC treatment was performed according to the established paradigm (10 mg/kg, i.p., twice a day for 6.5 days)[32], which evokes behavioral tolerance to classical cannabinoid effects and results in comparable THC blood levels in rodents to those observed after marijuana smoking in humans (~100 ng/ml)[16,33,34]. 3D-STORM imaging uncovered robust THC-induced CB_1-downregulation (74%) in perisomatic boutons (Fig. 6a-g) Furthermore, intracellular CB_1 ratio was significantly increased by 58% in THC-treated animals (Fig. 6h). Thus, chronic THC treatment has two, likely inter-related effects: a marked internalization and a dramatic disappearance of CB_1 receptors from the boutons.

Moreover, these results indicate that reduced CB_1 number on axon terminals underlies decreased cannabinoid effects on GABAergic currents after chronic THC administration.

Endocannabinoid signaling at GABAergic synapses sets the threshold for synaptic potentiation at nearby glutamatergic synapses[35,36]. Accordingly, chronic THC treatment prevents long-term potentiation (LTP) of excitatory synapses, which was postulated to be caused by functional tolerance to cannabinoid inhibition of GABA, but not glutamate release[16]. LTP only partially recovers after THC withdrawal and remains persistently weaker for weeks[16], which parallels slow, incomplete recovery in hippocampal cannabinoid binding density and in hippocampus-dependent memory deficits in clinical studies during THC abstinence[37,38]. Whether prolonged LTP and memory defects are associated with chronically reduced CB_1 numbers on inhibitory boutons has not yet been investigated. To monitor the time course of receptor recovery, CB_1 NLPs and internalization were measured 11.5 days after THC withdrawal, when classical cannabinoid behavioral effects have recovered[32], but significantly weaker hippocampal LTP still persists[16]. Notably, CB_1 NLP was 35% lower in chronic THC-treated mice compared to vehicle-treated animals (Fig. 6g), but there was no longer a significant difference in internalization (Fig. 6h). Importantly, presynaptic CB_1 numbers fully recovered by 6 weeks after drug treatment cessation (Fig. 6g).

Medical cannabis preparations are designed to achieve lower THC blood levels (~10 ng/ml) to avoid adverse psychoactive effects[39]. Therefore, the effects of a lower THC dose (1 mg/kg, i.p., twice a day for 6.5 days) were also tested, which results in similar drug levels in the blood and does not elicit overt behavioral effects in rodents[40]. 3D-STORM imaging revealed that 1 mg/kg THC decreased CB_1 numbers only slightly (16%, Fig. 6g), and no internalization was observed (Fig 6h). Thus, THC administration has dose-dependent effects on CB_1 quantity in GABAergic axon terminals, and the slow time course of receptor recovery may contribute to long-lasting neurophysiological changes in synaptic transmission. Finally, these experiments also illustrate the power of 3D-STORM imaging to study physiologically and pathophysiologically relevant molecular changes at the nanoscale within identified subcellular compartments of targeted cell types.

DISCUSSION

Understanding the fine-scale molecular organization associated with physiological or pathophysiological processes in the nervous system has been hindered by the difficulty of performing cell-type-, and synapse-specific molecular investigations in complex brain circuits. In the present study, we introduce a widely applicable, new approach based on STORM superresolution microscopy, which allows integrated analysis of morphological and physiological parameters of a targeted neuron with quantitative molecular imaging at its identified synapses. To support the widespread application of this rapid and versatile methodology, we have also developed new analysis approaches, which enable molecular distance and density measurements on subcellular compartments at the nanoscale. The novel methodology and the corresponding analysis tools were instrumental in (1) characterizing the abundance and nanoscale distribution of CB_1 cannabinoid receptors on GABAergic axon terminals; (2) uncovering cell-type-specific molecular differences in the active zones of

interneuron bouton types, which support distinct cannabinoid regulation of somatic and dendritic GABAergic inhibition; and (3) revealing the extent and time course of molecular changes induced by different doses of chronic THC treatment, which contribute to the functional tolerance in cannabinoid signaling efficiency at GABAergic synapses.

Methodological implications

Each brain circuit consists of numerous cell types, e.g. more than 20 types of GABAergic interneurons have been specified so far in the hippocampal CA1 subfield[1]. A stunning molecular diversity of the synapses connecting these various cell types supports the specific computing tasks of given brain circuits[3]. Synaptic protein abundance and spatial localization are precisely regulated by physiological or pathophysiological mechanisms in a cell-type- and synapse-specific manner. For example, hippocampal CB_1 receptor levels are elevated at GABAergic synapses, but are decreased at glutamatergic synapses in mouse and human epileptic samples[41,42]. In Fragile X syndrome, endocannabinoid-dependent synaptic plasticity is enhanced at GABAergic synapses[43,44], but absent at glutamatergic synapses due to a shift in the perisynaptic position of a major endocannabinoid-synthesizing enzyme[45]. These findings stressed the importance of cell-type- and synapse-specific approaches to make molecular analysis at the nanoscale level feasible.

Two methods are generally used to perform molecular investigations in complex brain circuits: electron and confocal microscopy. Labor-intensive electron microscopic studies use the required spatial resolution to disclose molecular changes in a mixed synapse population. However, the cellular identity of the respective excitatory and inhibitory synapses usually cannot be revealed by electron microscopy[41,42,45]. As significant benefits, we noted that tissue processing for STORM imaging was much faster, less laborious, permitted larger sample size, and led to higher labeling density than preembedding immunogold electron microscopy, and could still achieve a similar localization precision of the endogenous target protein. Confocal microscopy is optimal for simultaneous detection of multiple target proteins and cellular markers, but it does not have the necessary spatial resolution to obtain important molecular information at the nanoscale level. In the present study, we found that the localization precision achieved by STORM microscopy, which is about an order of magnitude greater than with confocal microscopy, is advantageous for various reasons. First of all, STORM imaging supported more precise bouton-specific sampling of CB_1 receptor localization data, which is important, because the accumulation of adjacent CB_1-positive axons forms dense meshworks and the source of collected photons often cannot be reliably determined - especially axially - by confocal microscopy. STORM imaging also revealed morphological parameters, such as bouton size, more accurately than confocal microscopy or electron microscopy, because it lacks the confounding factors of light diffraction or anisotropic shrinkage, respectively[22]. Furthermore, the improved localization precision of STORM enabled the separation of functionally different surface-associated versus intracellular receptor pools, as well as the measurement of their relative changes upon chronic THC treatment. Finally, and most importantly, STORM imaging made it possible for the first time to uncover the homogeneous CB_1 distribution pattern on the bouton surface, and the clustered organization of the release machinery component bassoon together with several quantitative parameters regarding their relative amounts and spatial

relationships in a cell-type-specific manner. The implications of these findings suggest that the receptor/effector ratio and distance at the nanoscale level are two important parameters, which affect the strength of synaptic endocannabinoid signaling. It is important to note here that other superresolution microscopy approaches, e.g. stimulated emission depletion microscopy, also permit correlated confocal and superresolution imaging[19]. However, single-molecule localization-microscopy provides better localization precision especially in the z-axis. This is required for the accurate molecular distribution data reported here, and offers better experimental flexibility for multicolor imaging, making it the method-of-choice for most neuroscience applications aiming for nanoscale localization of endogenous proteins.

Based on the above advantages demonstrated directly in the current study, we propose that STORM imaging combines the major strengths of electron and confocal microscopy, and, therefore represents a powerful approach to be applied for cell-type-specific molecular investigations in brain circuits. In summary, we introduced a series of innovations to this end, including i) the development of specific slice processing and immunostaining protocols to perform high-throughput STORM imaging of physiologically and morphologically characterized interneurons and to obtain excellent signal-to-noise STORM imaging data; ii) the combination of confocal and STORM microscopy to acquire correlated morphological and molecular data from the very same identified subcellular compartment of a target neuron; and iii) the generation of novel algorithms, data processing and analysis tools to make quantitative investigation of molecular densities and distances together with morphological parameters feasible at the nanoscale level within these subcellular compartments. We have provided cellular context to the previous ability to study proteins in random synapse populations[27] by using biocytin labeling and correlated confocal and STORM microscopy. The morphological details revealed here together with the multicolor feature of STORM imaging elucidated the precise position of CB_1 receptors in relation to the active zone and its reorganization after chronic THC treatment in a cell-type-specific manner. Importantly, our approach can be applied to other pre- or postsynaptically located molecular targets in any cell type and subcellular compartment in the future.

Biological implications

An important objective of our study was to ascertain molecular organizational properties that may influence cell-type-specific cannabinoid efficacy on neurotransmitter release. As an example, we studied perisomatically-projecting and dendritically-projecting hippocampal GABAergic interneurons, which exhibit marked differences in the strength of cannabinoid signaling[15]. The cell-type-specific approach identified unexpected organizational similarities and differences in the molecular architecture of cannabinoid-sensitive axon terminals belonging to these interneurons. In light of the accumulation of postsynaptic ionotropic receptors within precisely organized nanodomains[22-24], the homogeneous distribution of presynaptic CB_1 receptors shown by the polyhedron surface analysis is rather surprising. Dynamic ionotropic receptors are trapped in nanoclusters by postsynaptic anchoring proteins[22-24]. However, similar anchoring mechanisms for presynaptic CB_1 receptors have not yet been identified, despite the fact that other presynaptic GPCRs exhibit remarkable synaptic segregation patterns[46]. Interestingly, constitutive CB_1 trafficking is taking place

between the plasmalemmal surface of the pre-terminal axon and boutons[47], hence the homogeneous nanoscale distribution may be the consequence of unrestricted extrasynaptic receptor movement in the absence of specific anchoring mechanisms. Because homogeneous CB_1 distribution proved to be a common feature of perisomatic and dendritic CB_1-expressing bouton types, the subcellular distribution pattern of CB_1 receptors alone does not explain the quantitative physiological differences in cannabinoid signaling.

The correlation of confocal and STORM data also uncovered that larger boutons carry more presynaptic CB_1 receptors. It is widely accepted that the molecular topology of the active zone is precisely orchestrated[27,31]. Moreover, bigger axon terminals have larger total active zone areas, accommodating more VGCCs and other release machinery components[30]. The present observation adds to this view of the highly organized presynapse by demonstrating that the number of presynaptic regulatory receptors also scales with the size of the axon terminal in both examined interneuron types. This also underlines that CB_1 numbers on a given axon terminal type may be more related to the size of the bouton than to the identity of the cell type itself. Indeed, we found that identically sized perisomatic and dendritic boutons contain equal amounts of CB_1 receptors. Conversely, the number of the active zone protein bassoon seems to be affected by other factors as well, because significantly more bassoon were observed in dendritic terminals compared to perisomatic terminals with a similar size. It will be interesting to investigate in the future whether the somatodendritic location of a given synapse predicts bassoon number and the size of the corresponding active zone.

Considering the generally different position and function of perisomatic and dendritic GABAergic synapses on the somatodendritic surface of pyramidal neurons[1,14], the lower bassoon number in individual bassoon clusters in perisomatic boutons is an interesting finding. Because bassoon copy numbers correlate with the number of VGCC subunits[31], this observation raises the possibility that less N-type VGCCs (for which a sensitive and specific antibody is not yet available) are located at individual active zones in perisomatically-projecting interneurons. On the other hand, since we found that perisomatic boutons have more CB_1 receptors, which are uniformly distributed, a given VGCC/bassoon-containing release machinery may be regulated by more adjacent CB_1 receptors. In agreement with this prediction, the CB_1/bassoon ratio was 46% larger within 100 nm of the bassoon cluster edges in boutons belonging to perisomatically-projecting interneurons compared to axon terminals originating from dendritically-projecting cells. This is also consistent with the pharmacological findings that cannabinoid administration at low concentrations only inhibits GABA release from perisomatic interneurons[15]. Because saturating levels of cannabinoids are equally effective in reducing GABAergic transmission at both terminal types[15], it is conceivable that the synaptic concentration of endocannabinoid ligands and the signaling efficacy of presynaptic CB_1 receptors are the two principal factors, which together determine the strength of endocannabinoid signaling at a given synapse. However, one major implication of the quantitatively different nanoscale molecular organization of CB_1-containing interneuron terminals uncovered in the present study is that the nanoscale receptor/effector ratio and coupling distance, and not the total number of CB_1 receptors on a given axon terminal alone, determines how cannabinoid signaling controls neurotransmitter release.

CB_1 receptors mediate the acute psychoactive effects of cannabis preparations in humans[48] and chronic cannabis users exhibit strong, long-lasting cognitive deficits including impairments in hippocampus-dependent memory functions[37]. Our understanding of how acute and chronic cannabis consumption perturbs endocannabinoid signaling has been limited, as it was previously not technically possible to determine the underlying molecular changes within a particular compartment of a particular cell type. This is of special importance considering that chronic cannabis abuse triggers non-uniform loss of CB_1-specific radioligand binding sites in human brain regions[38]. In accordance with the circuit-specific effects, chronic THC administration causes strong reduction in cannabinoid efficacy selectively on GABAergic transmission[16], but until now the primary molecular mechanisms accounting for this reduction could not be directly investigated in identified GABAergic axon terminals. Our combined confocal/STORM approach enabled us to address this question and revealed an astonishing loss of presynaptic CB_1 receptors at the level of individual GABAergic boutons. The increased accumulation of intracellular (presumably internalized) receptors, together with the robust loss of receptors (probably due to protein degradation), indicate that the decreased availability of plasma membrane receptors reduces cannabinoid efficacy on GABA release upon chronic THC administration.

In light of the fact that classical cannabinoid effects are regained in mice 11.5 days after the last THC treatment[32], it was surprising that CB_1 receptors only partially recovered at this time point. However, hippocampal LTP is still significantly impaired after two weeks[16] and human memory deficits persist even after 28 days of abstinence[37]. These long-lasting neurophysiological and neurocognitive impairments may be influenced by the partial receptor retrieval, especially since CB_1 activation on GABAergic terminals underlies THC-induced long-term memory deficits[17,18], and sets the threshold for LTP at excitatory synapses[35,36]. Certainly, direct interpretations of findings obtained in mice and humans are difficult due to potentially different pharmacokinetics. Nevertheless, the dose (10mg/kg) applied here results in similar blood THC levels as observed in humans smoking marijuana with low THC content[33,34,49] and hippocampal CB_1 radioligand binding density did not show reversal in chronic daily marijuana users even after 4 weeks of abstinence[38]. Regarding this latter observation, it is important to note that CB_1 numbers returned to normal levels 6 weeks after cessation of THC administration. In addition, a low THC dose which is in the range used in medical applications[39,40] caused only minor loss of CB_1 receptors on GABAergic axon terminals. Considering the rapidly expanding considerations for the potential for THC-based medical treatments[50], and the increasing legal recreational use of cannabis preparations with rising THC concentrations[49], these findings have also important significance for a better understanding of the molecular adaptive responses associated with chronic THC exposure.

ONLINE METHODS

Maintenance, transfection and immunostaining of HEK293 cells

HEK293 cells were a kind gift from Dr. Balázs Gereben (Institute of Experimental Medicine, Budapest, Hungary). Cells were maintained under routine conditions in cell culture treated T25 flasks in high glucose-containing (25mM D-glucose) Dulbecco's

modified Eagle's medium supplemented with 10 % heat-inactivated neonatal calf serum at 37 °C and 5 % CO_2. Cultures were regularly tested for the presence of mycoplasma contamination via DAPI staining. Before transfection the cells were split onto poly-D-lysine (20 μg/ml) coated glass bottomed dishes. Transfection was performed using 1 μg of cDNA encoding an N-terminally EGFP-tagged CB_1 protein[51] and 1 μg Lipofectamine 2000 (Invitrogen) per dish, according to manufacturer's instructions. Dishes were maintained at 37 °C and 5 % CO_2 for at least 18 hrs to allow for efficient cDNA incorporation and protein expression. After incubation, cells were fixed in 4 % paraformaldehyde for 15 mins, washed three times in 0.1M PB, permeabilized in 0.1 % Triton X-100 in 0.05M TBS for 10 mins and immunostained with a primary antibody against CB_1 receptors (guinea pig anti-CB_1 antibody described in[52], 1μg/ml in TBS) for 1 hr. The cells were then washed in TBS three times and stained with a secondary antibody custom-made for STORM imaging (Cy3- and Alexa647-conjugated donkey anti-guinea pig antibody, 1:50 in TBS) for 1 hr. Cells were then washed twice each in TBS and PB. Immediately before STORM imaging, PB was removed and freshly prepared imaging medium (see below) was added to the dishes. Randomly selected HEK cells with heterogeneous expression levels were imaged and included in the analysis. Imaging conditions were identical to those used for tissue samples (detailed below).

Perfusion and preparation of tissue sections

All animal experiments were approved by the Hungarian Committee of the Scientific Ethics of Animal Research (license number: XIV-1-001/2332-4/2012), and were carried out according to the Hungarian Act of Animal Care and Experimentation (1998, XXVIII, Section 243/1998), which are in accordance with the European Communities Council Directive of 24 November 1986 (86/609/EEC; Section 243/1998). All efforts were made to minimize pain and suffering and to reduce the number of animals used. Adult male littermate $CB_1^{+/+}$ and $CB_1^{-/-}$ C57BL/6H mice[53] (kindly provided by Prof. Andreas Zimmer, University of Bonn, Germany) were deeply anesthetized with intraperitoneal injection of ketamine–xylazine (25 mg/ml ketamine, 5 mg/ml xylazine, 0.1% w/w pipolphen in H2O; 1 ml/100 g), then perfused transcardially with 0.9% saline for 2 mins, followed by 4% paraformaldehyde (PFA) in 0.1 M phosphate buffer (PB, pH 7.4) for 20 mins. After perfusion, the brains were removed from the skull, cut into blocks and incubated in 4% PFA for 2 hrs. Coronal sections of either 20 μm- or 50 μm-thickness for immunofluorescence labeling or for immunogold staining, respectively, were cut with a Leica (Nussloch, Germany) VT-1000S vibratome.

Immunogold staining

Pre-embedding immunostaining was performed using guinea pig anti-CB_1 primary antibody[52] (1 μg/ml) as described earlier[54]. Electron micrographs were taken with a Hitachi (Yokohama, Japan) H-7100 electron microscope.

For the quantification of CB_1-immunogold labeling, random cross-sections of immunogold-containing axon terminals forming symmetrical synapses were selected in either stratum pyramidale or stratum radiatum. After collecting images of 100–100 axon terminals in each layer and each animal (n = 3), the images were analyzed using ImageJ. The area of the axon

terminals was determined as the area of a freehand shape drawn along the plasma membrane. Preterminal axon segments were recognized based on their thin diameter and lack of synaptic vesicles, and were excluded from the analysis. Finally, the number of total and membrane-bound (center of particle within 50 nm from the plasma membrane) silver-intensified gold particles were counted on each terminal.

Acute slice preparation and recording

Coronal hippocampal slices (300 μm) were prepared from 25–30 days old male C57BL/6H $CB_1^{+/+}$ mice or $CB_1^{-/-}$ mice[53]. Slices were incubated in high sucrose-containing artificial cerebrospinal fluid (ACSF; in mM, 85 NaCl, 75 sucrose, 2.5 KCl, 25 glucose, 1.25 NaH_2PO_4, 4 $MgCl_2$, 0.5 $CaCl_2$, and 24 $NaHCO_3$) for 60 mins, and then transferred to a submerged recording chamber constantly perfused with oxygenated ACSF (containing in mM: 126 NaCl, 2.5 KCl, 26 $NaHCO_3$, 2 $CaCl_2$, 2 $MgCl_2$, 1.25 NaH_2PO_4, and 10 glucose, equilibrated with 95% O_2 and 5% CO_2). All electrophysiological recordings were performed at 33°C in the slice chamber of a fixed stage microscope (Nikon Eclipse FN1) and infrared differential interference contrast (DIC) optics was used to visualize the slices.

Whole-cell recordings were obtained using patch pipettes (3–4 MΩ) filled with internal solution containing (in mM) 126 K-gluconate, 4 KCl, 10 HEPES, 4 ATP-Mg, 0.3 GTP-Na, 10 phosphocreatine, and 0.2% biocytin, pH 7.2, 270–290 mOsm. Pyramidal cells and interneurons were located in the strata pyramidale and radiatum of the CA1 subfield in the hippocampus, respectively. Recordings were performed using MultiClamp700B amplifiers (Molecular Devices). Signals were filtered at 3 kHz using a Bessel filter and digitized at 10 kHz with a Digidata 1440A analog–digital interface (Molecular Devices). Series resistances were carefully monitored, and the recordings were discarded if the series resistance changed > 20% or reached 20 MΩ. The recorded traces were analyzed using the Clampfit 10.2 software (Molecular Devices). After ~30 mins of recording, the slices were fixed immediately in 4% PFA in 0.1 M PB for 40–48 hrs at 4 °C. All recorded regular-spiking cells were developed after fixation, but those interneurons whose axon arbor was not visualized by biocytin labeling-, or those which were found to be CB_1-immunonegative were excluded from the study.

In vivo recording

In vivo recordings were performed as described earlier[55], and were approved by the Institutional Animal Care and Use Committee of the University of California at Irvine. Briefly, a chronic head bar was implanted onto the skull of adult male C57BL/6 mice. After acclimation to the spherical treadmill apparatus, craniotomy surgery was performed, and borosilicate glass microelectrodes were lowered into the dorsal hippocampus. One electrode was used to record field potentials, while a second one was filled with Neurobiotin-containing solution (1.5–2% in 0.5% NaCl), and was used to perform juxtacellular recording and labeling of the recorded neuron.

Development and analysis of *in vitro* and *in vivo* recorded cells

After immersion fixation (in case of *in vitro* experiments) or after perfusion and slicing (in case of *in vivo* experiments), hippocampal sections were washed extensively in PB and 0.05

M Tris buffered saline (TBS, pH = 7.4), treated with 0.5% Triton X-100 in TBS twice for 30 mins, and incubated in Alexa488-Streptavidin (1:1000, Jackson ImmunoResearch, Suffolk, UK). Sections were then washed in TBS and PB, mounted on glass slides in Vectashield with DAPI (Vector Laboratories, Burlingame, CA), coverslipped, and sealed with nail polish. Low magnification stacks of filled neurons were collected from 300 μm-thick sections (*in vitro* experiments) or from 20 μm-thick sections (*in vivo* experiments) on a Nikon A1R confocal scan head coupled to a Nikon Ti-E inverted microscope using a CFI Plan Apo VC 20× objective (0.75 NA). After imaging, the sections were returned to PB and processed further.

The quantification of laminar bouton distribution in biocytin- or neurobiotin-filled cells was performed on maximal intensity z-projections in ImageJ. The two borders of the pyramidal layer were drawn, the minimal distance of each axonal varicosity was measured from the two lines marking the layer borders, and a relative position was calculated, where 0 is the center, and 1 is the thickness of the pyramidal layer. The bouton distribution index (BDI) was calculated from the from the mode and interquartile range of the relative positions ($BDI = \frac{0.5}{M * (Q3 - Q1)}$) to reflect the extent of accumulation of boutons in the pyramidal layer. Cells with BDI > 1 were included as perisomatic, and cells with BDI < 0.5 were included as dendritic cells in the study. Finally, some representative examples of the biocytin-filled interneurons were reconstructed from confocal image stack using Neurolucida 10 software.

Immunostaining for STORM imaging

Immersion-fixed 300 μm acute brain slices or 60 μm sections from perfused brains were embedded in 2% agarose in distilled water, and 20 μm-thick coronal sections were cut with a Leica VT-1000S Vibratome in PB. After slicing, the sections were immunostained in a free-floating manner. Following washing in TBS, and blocking with 1% HSA (albumin from human serum, Sigma) in TBS, the sections were incubated with affinity-purified primary antibodies in TBS overnight at room temperature on an orbital shaker. Primary antibodies used in this study were the following: guinea pig anti-CB_1, 1:1000 (described earlier[52], validated in CB_1-knockout mice in the present study); rabbit anti-CB_1, 1 μg/ml (described and validated in $CB_1^{-/-}$ mice in the present study; ImmunoGenes Kft); mouse anti-CCK, 1:3000 (#9303, CURE Gastroenteric Biology Center, Los Angeles, CA, USA); mouse anti-bassoon, 1:2000 (ab82958, Abcam, MA, USA; specificity validated in bassoon-knockout mice[57]). Sections were then washed in TBS and incubated with the appropriate commercial (Jackson ImmunoResearch) or STORM secondary antibodies (prepared using unlabeled affinity-purified anti-guinea pig, anti-rabbit or anti-mouse whole IgG antibodies (Jackson ImmunoResearch), according to the established protocol of Bates et al., 2007[57]) for 4 hrs. Sections used for single biocytin STORM imaging were developed with Alexa647-Streptavidin (1:1000, 4 hrs, Jackson ImmunoResearch) instead of the primary and secondary antibody incubations. After washing in TBS and PB, sections were mounted and dried on acetone-cleaned #1.5 borosilicate coverslips, and stored dry at 4 °C until imaging. Immediately before imaging, samples were covered with imaging medium freshly prepared according to Dani et al, 2010[27] containing 5% glucose, 0.1 M mercaptoethylamine, 1 mg/ml

glucose oxidase, and catalase (2.5 μl/ml of aqueous solution from Sigma, approximately 1500 U/ml final concentration) in Dulbecco's PBS (Sigma). Finally, coverslips were sealed with nail polish, and transferred into the microscope setup after 10 mins. STORM imaging was performed for up to 3 hrs after covering the specimens.

Preparation of the rabbit anti-CB_1 antibody

Transgenic rabbits (Tg) that have enhanced neonatal Fc receptor (FcRn) activity[58], as they carry and express one extra copy of the rabbit FcRn α-chain encoding gene (rabbit FCGRT) in addition to the endogenous rabbit FCGRT gene on New Zealand White rabbit genetic background were used in this study. These rabbits are coded as NZW Tg1 rabbit FCGRT (78), wherein 78 refers to the founder line. Tg rabbits and their wild-type (wt) littermates were housed in specified pathogen-free facility. All the treatments of rabbits in this research followed the guidelines of the Institutional Animal Care and Ethics Committee at ImmunoGenes Kft that operated in accordance with permissions 22.1/601/000/2009 and XIV-I-001/2086-4/2012 issued by the Food Chain Safety and Animal Health Directorate of the Government Office of Pest County, Hungary.

Tg and wt rabbits (3 months old female siblings) were intramuscularly immunized with a keyhole limpet hemocyanin (KLH)-conjugated polypeptide (CB_1: N'-MHRAAESCIKSTVKIAKVT MSVSTDTSAEAL-C') corresponding to amino acid residues 443-473 of the mouse CB_1 receptor. Animals were immunized with 200 μg CB_1 peptide-KLH conjugate (CB_1-KLH) in complete Freund's adjuvant and challenged multiple times with 100 μg of the conjugate in incomplete Freund's adjuvant. Sera containing anti-CB_1 were affinity purified with a SulfoLink Immobilization Kit for peptides (Thermo Scientific), according to manufacturer's instructions. Antigen-specific and total immunoglobulin levels were determined by ELISA measurements. The purified antibody from one of the FcRn Tg rabbits, which showed the highest sensitivity was selected and used in the experiments. The specificity of this antibody was validated in $CB_1^{-/-}$ animals.

Combined confocal/STORM image acquisition

STORM images and the correlated high-power confocal stacks were acquired via a CFI Apo TIRF 100× objective (1.49 NA) on a Nikon Ti-E inverted microscope equipped with a Nikon N-STORM system, a Nikon C2 confocal scan head and an Andor iXon Ultra 897 EMCCD (with a cylindrical lens for astigmatic 3D-STORM imaging[59]). The setup was controlled by Nikon NIS-Elements AR software with N-STORM module. For STORM imaging, a 300 mW laser was used (VFL-P-300-647, MPB Communications, Montreal, Canada), fiber-coupled to the laser board of the microscope setup. To obtain images, the field of view was selected based on the live EMCCD image under 488 nm illumination. A confocal stack (512×512×15 pixels, 78×78×150 nm resolution) was then collected using 488 nm excitation. The field of view of the confocal scan area and the EMCCD were set to be identical. Next, the tissue was bleached by scanning in the z axis while using maximal illumination from the 647 laser line. Finally, the STORM image was acquired using a STORM filter cube (Nikon) and the EMCCD. For single channel STORM imaging, 1000 cycles of 1 activator (low-power excitation at 561 nm or 405 nm for CB_1 and bassoon, respectively), and 3 reporter frames (high-power 647 nm excitation), 30 ms each, were

captured resulting in an imaging time of 2 minutes per image. For dual channel STORM imaging, 1000 cycles of 8×30ms frames were captured, each cycle consisted of: 1 activator (405 nm), 3 reporter (647 nm), 1 activator (561 nm), and 3 reporter (647 nm) frames resulting in an imaging time of 4 minutes per image. The applied activator laser power was determined to be low enough to avoid extensively overlapping localizations, while the reporter laser power was always set to maximum. For dual-channel direct STORM imaging, a green/far-red dual filter cube (Nikon) was used, and each of the 10,000 imaging cycle consisted of 4–4 frames illuminated by either the 488 or the 647 laser lines at maximal power, while using continous low-power 405 nm illumination for activation. To minimize out-of-focus background, oblique illumination was applied using the TIRF illuminator of the microscope. Localization points were collected within 300–300 nm axial distances from the center plane of the bouton at a similar tissue depth (~5 μm) for all boutons to equalize antibody penetration probabilities and the impact of light scattering.

According to the established definition[60], we use the term localization precision to refer to the distribution of the position of the same fluorophore calculated from multiple separate images, and report the standard deviation of this distribution as localization precision values. Localization precision in STORM images obtained from the HEK cells and from hippocampal sections were determined from isolated clusters (n = 50-50) of localization points representing multiple detections of the same fluorophore.

Combined confocal/STORM image processing

All confocal image stacks of filled boutons were deconvolved with 40 iterations of the Classic Maximum Likelihood Estimation algorithm in Huygens software (SVI, The Netherlands). To register with correlated STORM images acquired on EMCCD, deconvolved confocal images were transformed using affine transformation by the TurboReg plugin in ImageJ[61]. The parameters of the required transformation were determined from reference image pairs of 100 nm fluorescent beads captured by both cameras.

STORM images were processed to acquire coordinates of localization points using the N-STORM module in NIS-Elements AR software. Identical settings were used for every image. To exclude camera noise, the peak detection threshold was set to 2500 gray levels(1200 photons). Calibration of 3D-STORM was performed according to the manufacturer’s instructions using a piezo stage controller (Nano-Drive, Mad City Labs) and 100 nm fluorescent beads immobilized oncoverslips. In case of dual channel STORM images, crosstalk subtraction was applied, using the same threshold settings for every image. The batch processing of images was solved using scripts written in Python and AutoHotkey to control NIS-Elements.

Correlation of confocal and STORM images was performed using custom-written macros in ImageJ. The boutons to be included in the analysis were selected from the deconvolved confocal image of the biocytin signal (maximum intensity z projection of 3 image planes centered at the plane corresponding to the focal plane of the STORM image), resampled to 1 nm/pixel resolution and localization points from the STORM data were overlaid on the image. When necessary, the confocal image was translated manually to fit the STORM data

acquired on the EMCCD sensor. In the case of CB_1 staining, the confocal image was fitted to the STORM image, as the CB_1 receptor-immunostaining is dense enough to outline the membrane of the bouton. In the case of single bassoon-immunostaining, the confocal image was fitted to the epifluorescence image of the bouton recorded on the EMCCD.

Visualization of STORM data were obtained by using the N-STORM module in NIS-Elements AR for 2D images and by using the Visual Molecular Dynamics (VMD) software for 3D renderings. The 3D localization coordinates were converted to PDB (Protein Data Bank) file format. Each STORM channel was assigned to a different chain identifier or atomic type in order to visualize by VMD 1.8.7. The convex hull edges, as well as shortest-distance trajectories, were visualized as chemical bonds (see below).

Quantitative analysis of combined confocal/STORM images of axon terminals

To avoid any potential bias in assigning a given localization point to a given bouton, a freehand shape was first drawn around the center plane of the biocytin-filled bouton on the confocal image. Bouton size was measured as the area of the shape. Shape descriptors were measured using the built-in measurement functions of ImageJ. Next, the STORM localization points (LPs) belonging to the particular bouton were determined. In the specific case of CB_1- CCK double immunostaining comparison in wild-type and CB_1 knockout mice, rectangules were placed onto the CCK-immunopositive boutons. The coordinates of localizations within the selected volume were saved for further analysis. The perimeter of the bouton was determined as the perimeter of a 2D-convex hull fitted on the CB_1 localizations.

For the measurement of surface distances, a tri-dimensional convex hull was fitted onto the outermost CB_1 localizations, and the shortest distance between two localizations on the surface of this polyhedron was determined. First, we approximated the bouton surface by calculating the 3D-convex hull of the CB_1 localizations belonging to a single biocytin-filled bouton using Matlab software (Mathworks). Localization points were projected onto the surface by determining the nearest point of the convex hull. To avoid possible problems arising from projection to a wrong face, internal localizations with a distance of more than 80 nm from the surface were rejected from the analysis. A second convex hull was fitted on the bassoon LPs, and the nearest point “Q” on the surface of this polyhedron to each CB_1 localization point “P1” was determined. This point Q was then projected onto the bouton surface by determining the point “P2” of the CB_1 convex hull which is nearest to Q. Given the two points P1 and P2, the shortest route between P1 and P2 on the surface of the bouton was approximated by the following algorithm. An axis was defined by connecting P1 and P2. If any half-plane S is fit on this axis then S intersects the surface of the convex hull in a path connecting P1 and P2. This path can be determined explicitly by the points of intersection of S and the edges of the convex hull. Hence the length of this route is also explicitly computable for each S. Finally, we rotated S around the axis degree-by-degree, and the minimum of the arising trajectories was assumed as the approximately shortest route between P1 and P2 on the surface of the convex hull.

For the measurement of CB_1 localization point densities, random points of the hull surface were first selected at a high density. Afterwards, the number of CB_1 localization points

within 200 nm from each point was determined together with the surface distance of each measurement point from the nearest point of a convex hull fitted onto the bassoon localization points.

For the measurements of bassoon localization point clusters, we implemented the widely used Density-Based Spatial Clustering of Applications with Noise[62] (DBSCAN) in Matlab. This method finds dense clusters in a set of 3D points with the advantage that there is no need to define *a priori* number of clusters.. A point P is considered as a member of a cluster, if it has at least MinP number of neighbors within epsilon, while P is considered as noise otherwise. All 21 possible combinations of several settings of the epsilon (50 to 150nm) and minP (2 to 4) parameters of the algorithm were run on the data, and yielded similar results. Data are shown for the epsilon = 100 nm and minP = 3 setting.

Detecting multiple blinkings of the same fluorophore can potentially lead to artificial clustering of signal in single-molecule localization-based superresolution microscopy data[63]. However, the following three measurements and observations indicate that the detected clusters represent bassoon distribution and cannot be explained by multiple detections of fluorophores or apperent clustering of randomly distributed signal. First of all, the vast majority of detected fluorophores blinked only once during the time of the imaging (~80%), as images of isolated fluorophores appeared as single localizations, and rarely as doublets or triplets, while the bassoon clusters typically comprised of 10–20 localization points (on average 15.46). Secondly, the size of bassoon clusters were much larger than the distribution of multiple localizations of single fluorophores. While the mean diameter of a bassoon cluster was 201 nm, the distribution of multiple localizations of isolated fluorophores was restricted to 40 nm diameter (Supplementary Figure 2a-c). Thirdly, when the same clustering analysis was performed on data from ROIs taken from pyramidal cell nuclei then the analysis could not reproduce a cluster/noise ratio or cluster size distribution specific for data from ROIs obtained from axon terminals.

To discern whether given molecular parameters are related to axon terminal size or represent cell-type-specific features, we analyzed two samples of boutons with identical size distribution from both interneuron types. The samples were generated by picking an equal number of boutons from each cell type from within the interdecile range of bouton sizes of the given cell type, at random. Then, for each bouton, a corresponding second bouton, which exhibited the least difference in size and which was not yet included in the sample was identified among boutons of the other cell type.

Chronic drug treatment

All procedures were performed in accordance with the Italian Ministry of Health guidelines (D.L. 116/92; D.L. 111/94-B) and EEC Council Directives (219/1990 and 220/1990). All efforts were made to minimize pain and suffering and to reduce the number of animals used. Male C57BL/6J mice (Harlan, Italy), 22–31 days of age at the beginning of the treatments, were housed (ten per cage) in a controlled environment at constant temperature (21±1°C) and humidity (60%) on a 12-h light–dark cycle (lights on at 7.00 a.m.),with free access to food and water. Animals were grouped in a randomized manner and treated either with Δ^9-tetrahydrocannabinol (THC) or its vehicle intraperitoneally at a dose of 10 mg/kg (i.p.

injection volume of 10 ml/kg) twice a day for 6.5 days. THC (THC-Pharm GmbH, Germany) was dissolved in a solution containing 1% ethanol, 2% Tween 80 and saline. This chronic treatment regimen was shown to induce behavioral tolerance in mice[32,64]. From the six experimental groups, in the first and second groups, twenty-four hrs after the last THC or vehicle injection, respectively, mice were anesthetized with isoflurane and acute slices were cut to perform electrophysiological recordings as described above. In the third and fourth groups, the same process was carried out 11.5 days after cessation of THC or vehicle administration, respectively. In the fifth and sixth groups, the same process was performed 6 weeks after THC withdrawal or vehicle treatment, respectively. In a separate experiment, two groups of mice received either a subthreshold dose of THC (1 ml/kg, i.p.,), which does not elicit classical behavioral effects of cannabinoids[40], or vehicle twice a day for 6.5 days and electrophysiological recordings were done twenty-four hrs after finishing the treatment protocol. All recordings, developments, stainings, imaging, and analyses of samples were conducted by experimenters blinded to treatment.

Internalization measurements

Due to the reduced number of localization points after chronic THC administration, using the CB_1 convex hull as the approximation of the bouton surface could lead to an underestimated measure of internalization. To overcome this problem, an internalization index was calculated. First, the distance (d) of each CB_1 localization points was measured from the 3D center of mass of all localization points within the given axon terminal. The radius of the terminal was estimated from the area measured on the biocytin confocal image of the bouton, assuming a circular shape (r). Finally, the d/r ratio of every localization point was averaged for each bouton. This measure is sensitive to a shift of the localizations towards the center of the bouton. To estimate the extent of internalization, we first measured the ratio of membrane over total receptors in untreated animals using immunogold electron microscopy (88% for perisomatic interneurons). Subsequently, we determined a d/r threshold for individual localization points to get the same ratio from the STORM data of control perisomatic axon terminals. Finally, we assessed internalization in the data from boutons derived from THC-treated mice using the established d/r threshold.

Statistical analysis and figure preparation

Statistical analysis was performed and graphs were generated using STATISTICA 11 software (StatSoft, Tulsa, OK). Based on bouton size, outlier boutons were excluded if two-sided Grubb's test ($\alpha = 0.05$) indicated the presence of outliers within the given cell. Each data set was tested for normality using Kolmogorov-Smirnov test, and for differences between animals or cells using Kruskal-Wallis test, before the appropriate statistical method was determined. Boutons from different animals were pooled if there was no significant difference between animals or cells of any group (Kruskal-Wallis test, $p > 0.05$). Otherwise, the mean values of individual animals or cells were used. Data always met the assumptions of the applied statistical probes. An estimate for the variance in data obtained with our approach was not available, thus no statistical methods were used to establish the number of samples analyzed. Post-hoc power analysis indicated that with our measured variance in NLP, mean values from 6 animals, or 70 pooled boutons per group are required to detect a

25% standardized effect size between groups with 0.8 power and 0.05 alpha using two-tailed t test.

Figures were prepared using Photoshop CS5 (Adobe Systems, San Jose, CA). All images were modified in exactly the same way for all groups or genotypes during preparation of the figures to ensure equal comparison of animals from different treatment groups or genotypes, and comparison of cell types. A supplementary methods checklist is available.

Supplementary Material

Refer to Web version on PubMed Central for supplementary material.

ACKNOWLEDGMENTS

This study was primarily supported by the European Research Council Grant 243153 and by the Momentum Program (LP2013-54/2013) of the Hungarian Academy of Sciences to I.Katona. The project was also funded by the Hungarian Academy of Sciences Equipment Grant (IF-22/2012) for superresolution microscopy. I.Katona is a recipient of the Wellcome Trust International Senior Research Fellowship (090946/Z/09/Z). Additional support was provided by NIH (NS74432) to I.S., and by the Italian Ministry of University (Grant PRIN 2009: 200928EEX4) and “Fondazione Banco di Sardegna” to M.P. We are grateful to E. Tischler and G. Goda for their excellent technical assistance; to I. Mihály for bouton distribution analysis; and to C. Cserép and C. Fekete for their help with immunostaining and antibody labeling protocols. The authors are indebted to A. Zimmer for providing the CB_1 knockout mouse line and to A. Tímár for his help with software analysis. We also thank N. Hájos, N. Holderith, N. Lenkey and Z. Nusser for their comments on the manuscript. The help of the Nikon Microscopy Center at Institute of Experimental Medicine, Nikon Europe B.V., Nikon Austria GmbH and Auro-Science Consulting, Ltd is greatly acknowledged for kindly providing microscopy support.

REFERENCES

1. Klausberger T, Somogyi P. Neuronal diversity and temporal dynamics: the unity of hippocampal circuit operations. Science. 2008; 321:53–57. [PubMed: 18599766]
2. Lichtman JW, Denk W. The big and the small: challenges of imaging the brain’s circuits. Science. 2011; 334:618–623. [PubMed: 22053041]
3. O’Rourke NA, Weiler NC, Micheva KD, Smith SJ. Deep molecular diversity of mammalian synapses: why it matters and how to measure it. Nat Rev Neurosci. 2012; 13:365–379. [PubMed: 22573027]
4. Hangya B, Pi HJ, Kvitsiani D, Ranade SP, Kepecs A. From circuit motifs to computations: mapping the behavioral repertoire of cortical interneurons. Curr Opin Neurobiol. 2014; 26:117–124. [PubMed: 24508565]
5. Choquet D, Triller A. The dynamic synapse. Neuron. 2013; 80:691–703. [PubMed: 24183020]
6. Kano M, Ohno-Shosaku T, Hashimotodani Y, Uchigashima M, Watanabe M. Endocannabinoid-mediated control of synaptic transmission. Physiol Rev. 2009; 89:309–380. [PubMed: 19126760]
7. Katona I, Freund TF. Multiple functions of endocannabinoid signaling in the brain. Annu Rev Neurosci. 2012; 35:529–558. [PubMed: 22524785]
8. Lovinger DM. Presynaptic modulation by endocannabinoids. Handb Exp Pharmacol. 2008; 184:435–477. [PubMed: 18064422]
9. Katona I, et al. Presynaptically located CB1 cannabinoid receptors regulate GABA release from axon terminals of specific hippocampal interneurons. J Neurosci. 1999; 19:4544–4558. [PubMed: 10341254]
10. Wilson RI, Nicoll RA. Endogenous cannabinoids mediate retrograde signalling at hippocampal synapses. Nature. 2001; 410:588–592. [PubMed: 11279497]
11. Ohno-Shosaku T, Maejima T, Kano M. Endogenous cannabinoids mediate retrograde signals from depolarized postsynaptic neurons to presynaptic terminals. Neuron. 2001; 29:729–738. [PubMed: 11301031]

12. Klausberger T, et al. Complementary roles of cholecystokinin- and parvalbumin-expressing GABAergic neurons in hippocampal network oscillations. J Neurosci. 2005; 25:9782–9793. [PubMed: 16237182]
13. Tricoire L, et al. A blueprint for the spatiotemporal origins of mouse hippocampal interneuron diversity. J Neurosci. 2011; 31:10948–10970. [PubMed: 21795545]
14. Miles R, Toth K, Gulyas AI, Hajos N, Freund TF. Differences between somatic and dendritic inhibition in the hippocampus. Neuron. 1996; 16:815–823. [PubMed: 8607999]
15. Lee SH, Földy C, Soltesz I. Distinct endocannabinoid control of GABA release at perisomatic and dendritic synapses in the hippocampus. J Neurosci. 2010; 30:7993–8000. [PubMed: 20534847]
16. Hoffman AF, Oz M, Yang R, Lichtman AH, Lupica CR. Opposing actions of chronic Delta9-tetrahydrocannabinol and cannabinoid antagonists on hippocampal long-term potentiation. Learn Mem. 2007; 14:63–74. [PubMed: 17202425]
17. Puighermanal E, et al. Cannabinoid modulation of hippocampal long-term memory is mediated by mTOR signaling. Nat Neurosci. 2009; 12:1152–1158. [PubMed: 19648913]
18. Puighermanal E, et al. Dissociation of the pharmacological effects of THC by mTOR blockade. Neuropsychopharmacology. 2013; 38:1334–1343. [PubMed: 23358238]
19. Maglione M, Sigrist SJ. Seeing the forest tree by tree: super-resolution light microscopy meets the neurosciences. Nat Neurosci. 2013; 16:790–797. [PubMed: 23799471]
20. Rust MJ, Bates M, Zhuang X. Sub-diffraction-limit imaging by stochastic optical reconstruction microscopy (STORM). Nat Methods. 2006; 3:793–795. [PubMed: 16896339]
21. Vida I, Halasy K, Szinyei C, Somogyi P, Buhl EH. Unitary IPSPs evoked by interneurons at the stratum radiatum-stratum lacunosum-moleculare border in the CA1 area of the rat hippocampus in vitro. J Physiol. 1998; 506:755–773. [PubMed: 9503336]
22. MacGillavry HD, Song Y, Raghavachari S, Blanpied TA. Nanoscale scaffolding domains within the postsynaptic density concentrate synaptic AMPA receptors. Neuron. 2013; 78:615–622. [PubMed: 23719161]
23. Nair D, et al. Super-resolution imaging reveals that AMPA receptors inside synapses are dynamically organized in nanodomains regulated by PSD95. J Neurosci. 2013; 33:13204–13224. [PubMed: 23926273]
24. Specht CG, et al. Quantitative nanoscopy of inhibitory synapses: counting gephyrin molecules and receptor binding sites. Neuron. 2013; 79:308–321. [PubMed: 23889935]
25. Hefft S, Jonas P. Asynchronous GABA release generates long-lasting inhibition at a hippocampal interneuron-principal neuron synapse. Nat Neurosci. 2005; 8:1319–1328. [PubMed: 16158066]
26. Wilson RI, Kunos G, Nicoll RA. Presynaptic specificity of endocannabinoid signaling in the hippocampus. Neuron. 2001; 31:453–462. [PubMed: 11516401]
27. Dani A, Huang B, Bergan J, Dulac C, Zhuang X. Superresolution imaging of chemical synapses in the brain. Neuron. 2010; 68:843–856. [PubMed: 21144999]
28. Frank T, et al. Bassoon and the synaptic ribbon organize Ca^{2}+ channels and vesicles to add release sites and promote refilling. Neuron. 2010; 68:724–738. [PubMed: 21092861]
29. Herlitze S, et al. Modulation of Ca2+ channels by G-protein beta gamma subunits. Nature. 1996; 380:258–262. [PubMed: 8637576]
30. Holderith N, et al. Release probability of hippocampal glutamatergic terminals scales with the size of the active zone. Nat Neurosci. 2012; 15:988–997. [PubMed: 22683683]
31. Wilhelm BG, et al. Composition of isolated synaptic boutons reveals the amounts of vesicle trafficking proteins. Science. 2014; 344:1023–1028. [PubMed: 24876496]
32. Bass CE, Martin BR. Time course for the induction and maintenance of tolerance to Delta(9)-tetrahydrocannabinol in mice. Drug Alcohol Depend. 2000; 60:113–119. [PubMed: 10940538]
33. Heishman SJ, Huestis MA, Henningfield JE, Cone EJ. Acute and residual effects of marijuana: profiles of plasma THC levels, physiological, subjective, and performance measures. Pharmacol Biochem Behav. 1990; 37:561–565. [PubMed: 1965045]
34. Varvel SA, et al. Delta9-tetrahydrocannbinol accounts for the antinociceptive, hypothermic, and cataleptic effects of marijuana in mice. J Pharmacol Exp Ther. 2005; 314:329–337. [PubMed: 15831444]

35. Carlson G, Wang Y, Alger BE. Endocannabinoids facilitate the induction of LTP in the hippocampus. Nat Neurosci. 2002; 5:723–724. [PubMed: 12080342]
36. Chevaleyre V, Castillo PE. Endocannabinoid-mediated metaplasticity in the hippocampus. Neuron. 2004; 43:871–881. [PubMed: 15363397]
37. Bolla KI, Brown K, Eldreth D, Tate K, Cadet JL. Dose-related neurocognitive effects of marijuana use. Neurology. 2002; 59:1337–1343. [PubMed: 12427880]
38. Hirvonen J, et al. Reversible and regionally selective downregulation of brain cannabinoid CB1 receptors in chronic daily cannabis smokers. Mol Psychiatry. 2012; 17:642–649. [PubMed: 21747398]
39. Stott CG, White L, Wright S, Wilbraham D, Guy GW. A phase I study to assess the single and multiple dose pharmacokinetics of THC/CBD oromucosal spray. Eur J Clin Pharmacol. 2013; 69:1135–1147. [PubMed: 23179176]
40. DeLong GT, Wolf CE, Poklis A, Lichtman AH. Pharmacological evaluation of the natural constituent of Cannabis sativa, cannabichromene and its modulation by Δ(9)-tetrahydrocannabinol. Drug Alcohol Depend. 2010; 112:126–133. [PubMed: 20619971]
41. Chen K, et al. Long-term plasticity of endocannabinoid signaling induced by developmental febrile seizures. Neuron. 2003; 39:599–611. [PubMed: 12925275]
42. Ludányi A, et al. Downregulation of the CB1 cannabinoid receptor and related molecular elements of the endocannabinoid system in epileptic human hippocampus. J Neurosci. 2008; 28:2976–2990. [PubMed: 18354002]
43. Maccarrone M, et al. Abnormal mGlu 5 receptor/endocannabinoid coupling in mice lacking FMRP and BC1 RNA. Neuropsychopharmacology. 2010; 35:1500–1509. [PubMed: 20393458]
44. Zhang L, Alger BE. Enhanced endocannabinoid signaling elevates neuronal excitability in fragile X syndrome. J Neurosci. 2010; 30:5724–5729. [PubMed: 20410124]
45. Jung KM, et al. Uncoupling of the endocannabinoid signalling complex in a mouse model of fragile X syndrome. Nat Commun. 2012; 3:1080. [PubMed: 23011134]
46. Shigemoto R, et al. Target-cell-specific concentration of a metabotropic glutamate receptor in the presynaptic active zone. Nature. 1996; 381:523–525. [PubMed: 8632825]
47. Mikasova L, Groc L, Choquet D, Manzoni OJ. Altered surface trafficking of presynaptic cannabinoid type 1 receptor in and out synaptic terminals parallels receptor desensitization. Proc Natl Acad Sci U S A. 2008; 105:18596–18601. [PubMed: 19015531]
48. Huestis MA, et al. Blockade of effects of smoked marijuana by the CB1-selective cannabinoid receptor antagonist SR141716. Arch Gen Psychiatry. 2001; 58:322–328. [PubMed: 11296091]
49. Volkow ND, Baler RD, Compton WM, Weiss SR. Adverse health effects of marijuana use. N Engl J Med. 2014; 370:2219–2227. [PubMed: 24897085]
50. Pertwee RG. Targeting the endocannabinoid system with cannabinoid receptor agonists: pharmacological strategies and therapeutic possibilities. Philos Trans R Soc Lond B Biol Sci. 2012; 367:3353–3363. [PubMed: 23108552]

REFERENCES FOR ONLINE METHODS

51. Tappe-Theodor A, et al. A molecular basis of analgesic tolerance to cannabinoids. J Neurosci. 2007; 27:4165–4177. [PubMed: 17428994]
52. Fukudome Y, et al. Two distinct classes of muscarinic action on hippocampal inhibitory synapses: M2-mediated direct suppression and M1/M3-mediated indirect suppression through endocannabinoid signalling. Eur J Neurosci. 2004; 19:2682–2692. [PubMed: 15147302]
53. Zimmer A, Zimmer AM, Hohmann AG, Herkenham M, Bonner TI. Increased mortality, hypoactivity, and hypoalgesia in cannabinoid CB1 receptor knockout mice. Proc Natl Acad Sci U S A. 1999; 96:5780–5785. [PubMed: 10318961]
54. Nyilas R, et al. Enzymatic machinery for endocannabinoid biosynthesis associated with calcium stores in glutamatergic axon terminals. J Neurosci. 2008; 28:1058–1063. [PubMed: 18234884]
55. Varga C, Golshani P, Soltesz I. Frequency-invariant temporal ordering of interneuronal discharges during hippocampal oscillations in awake mice. Proc Natl Acad Sci U S A. 2012; 109:E2726–2734. [PubMed: 23010933]

56. Dick O, et al. The presynaptic active zone protein bassoon is essential for photoreceptor ribbon synapse formation in the retina. Neuron. 2003; 37:775–786. [PubMed: 12628168]

57. Bates M, Huang B, Dempsey GT, Zhuang X. Multicolor super-resolution imaging with photo-switchable fluorescent probes. Science. 2007; 317:1749–1753. [PubMed: 17702910]

58. Baranyi M, Cervenak J, Bender B, Kacskovics I. Transgenic rabbits that overexpress the neonatal Fc receptor (FcRn) generate higher quantities and improved qualities of anti-thymocyte globulin (ATG). PLoS One. 2013; 8:e76839. [PubMed: 24194847]

59. Huang B, Wang W, Bates M, Zhuang X. Three-dimensional super-resolution imaging by stochastic optical reconstruction microscopy. Science. 2008; 319:810–813. [PubMed: 18174397]

60. Deschout H, et al. Precisely and accurately localizing single emitters in fluorescence microscopy. Nat Methods. 2014; 11:253–266. [PubMed: 24577276]

61. Thévenaz P, Ruttimann UE, Unser M. A pyramid approach to subpixel registration based on intensity. IEEE Trans Image Process. 1998; 7:27–41. [PubMed: 18267377]

62. Ester, M.; Kriegel, H-P.; Sander, J.; Xu, X. A density-based algorithm for discovering clusters in large spatial databases with noise. Proceedings of the Second International Conference on Knowledge Discovery and Data Mining (KDD-96); 1996; p. 226-231.

63. Veatch SL, et al. Correlation functions quantify super-resolution images and estimate apparent clustering due to over-counting. PLoS One. 2012; 7:e31457. [PubMed: 22384026]

64. McKinney DL, et al. Dose-related differences in the regional pattern of cannabinoid receptor adaptation and in vivo tolerance development to delta9-tetrahydrocannabinol. J Pharmacol Exp Ther. 2008; 324:664–673. [PubMed: 17967938]

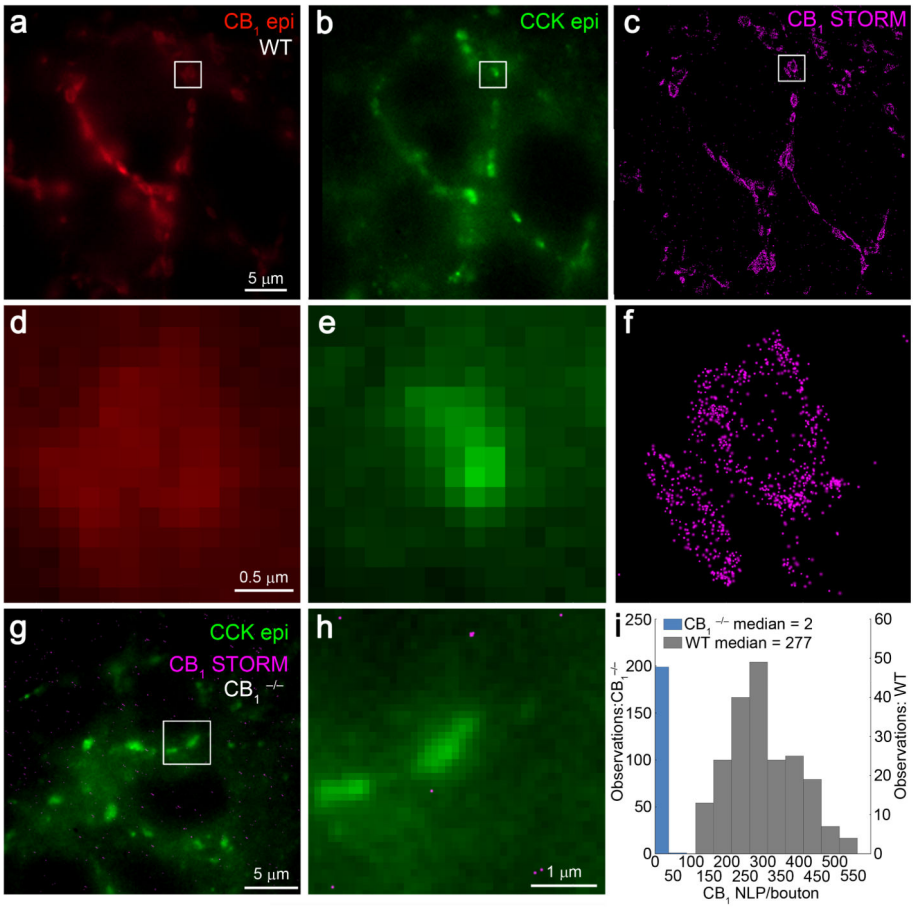

Figure 1. 3D-STORM imaging of CB_1 receptors on hippocampal GABAergic axon terminals

(**a**) Immunofluorescence labeling of CB_1 receptors in the CA1 stratum pyramidale of $CB_1^{+/+}$ mice showed basket-like arrangement of CB_1-positive axon terminals encircling a CB_1-immunonegative pyramidal cell somata. (**b**) These axon terminals could also be visualized by immunofluorescence staining for the neuropeptide CCK, a neurochemical marker of CB_1-expressing interneurons. (**c**) STORM imaging of CB_1 receptors revealed identical basket-like orientation of the same perisomatic GABAergic axon terminals. (**d,e**) Magnifying the epifluorescence images failed to delineate the morphological structure of the respective profiles located in the boxed region or the precise nanoscale position of CB_1 receptors with the axon terminals. (**f**) In contrast, the improved spatial resolution of 3D-STORM microscopy made it possible to reliably discern individual CB_1-positive boutons located adjacently to one another, as well as to reveal localization points representing the nanoscale position of CB_1 receptors. (**g,h**) To validate the specificity of our approach, hippocampal sections from littermate $CB_1^{-/-}$ mice were also processed and imaged under the same conditions. In these sections, we found an almost complete absence of STORM localization points representing CB_1 within CCK-immunolabeled boutons. (**i**) Histogram of CB_1 NLP in individual CCK-positive varicosities in the CA1 stratum pyramidale of sections derived from littermate $CB_1^{+/+}$ (n = 3 animals; n = 208 axon terminals) or $CB_1^{-/-}$ (n = 2 animals; n = 200 axon terminals) mice. Note that the drastically reduced CB_1 NLP value in

$CB_1^{-/-}$ samples validates the specificity of the antibody, the staining process and the STORM imaging protocol.

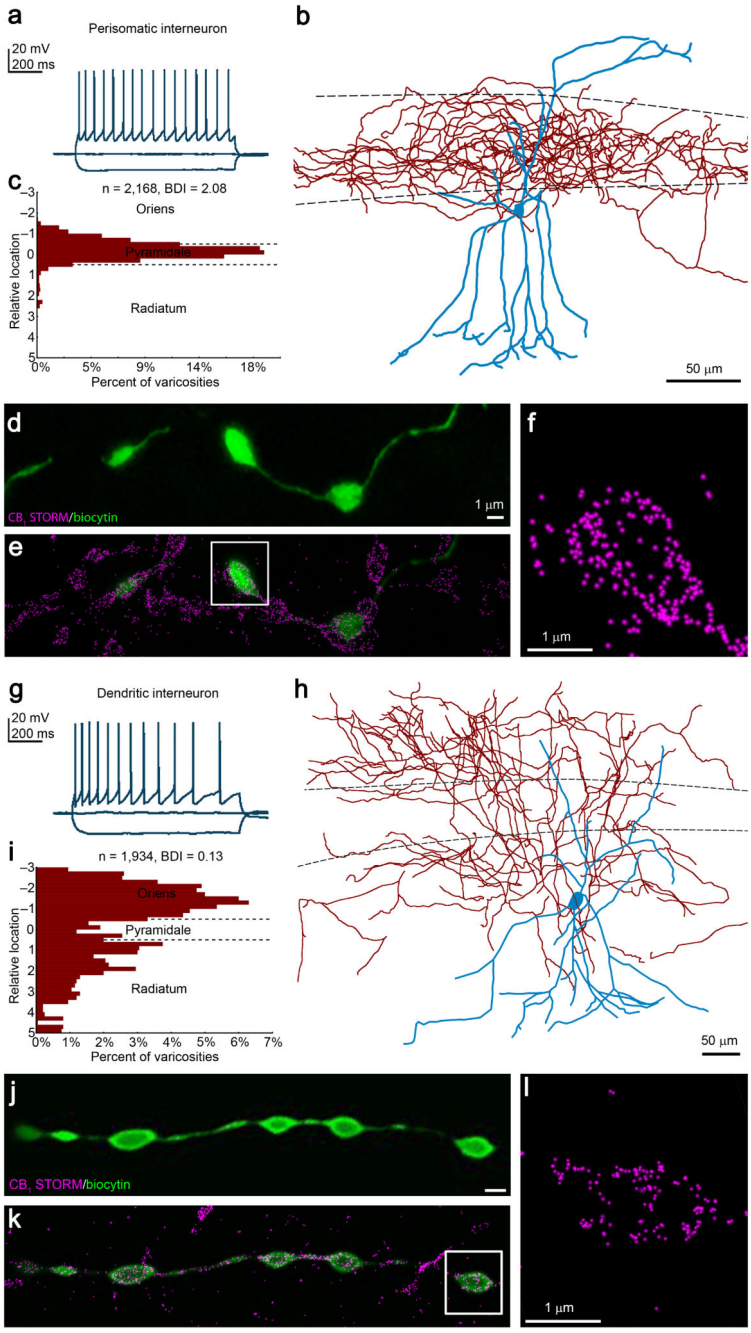

Figure 2. Cell-type-specific integrated analysis of physiological properties, anatomical parameters and nanoscale molecular imaging

(**a**) Representative voltage traces in response to depolarizing and hyperpolarizing current steps recorded in whole-cell patch-clamp configuration from a multipolar neuron in CA1 stratum radiatum shows the characteristic accommodating, regular-spiking pattern. (**b**) The neuron was filled with biocytin during recording to allow post-hoc reconstruction. While the dendrites (blue) arborize in all hippocampal layers, the axon cloud (red) is restricted to the stratum pyramidale. (**c**) Measurement of the relative laminar location of the recovered axonal varicosities confirms a bouton distribution biased towards the pyramidal layer. The

bouton distribution index (BDI) based on the descriptive statistics of the distance distribution classifies this cell as a perisomatic interneuron (BDI > 1). (**d**) Maximum intensity projection of a deconvolved confocal stack of the biocytin-filled axon terminals. (**e,f**) Subsequent STORM superresolution imaging reveals CB_1-immunolabeling on the identified boutons. (**f**) This STORM image depicts CB_1 receptor localization points within the axon terminal shown in the boxed region in d_2. (**g**) Traces recorded from another interneuron also show accommodating firing pattern. (**h**) This multipolar interneuron exhibits a distinct axonal morphology from the cell presented in b. (**i**) BDI classifies this cell as a dendritic interneuron (BDI < 0.5). (**j-l**) Combined confocal/STORM imaging visualizes the nanoscale distribution of CB_1 receptors in identified boutons of the same dendritic interneuron. Boutons were imaged at a similar tissue depth (~5 μm) to equalize antibody penetration probability and the impact of light scattering. Throughout the present study, we have processed and evaluated 80 interneurons in the same manner.

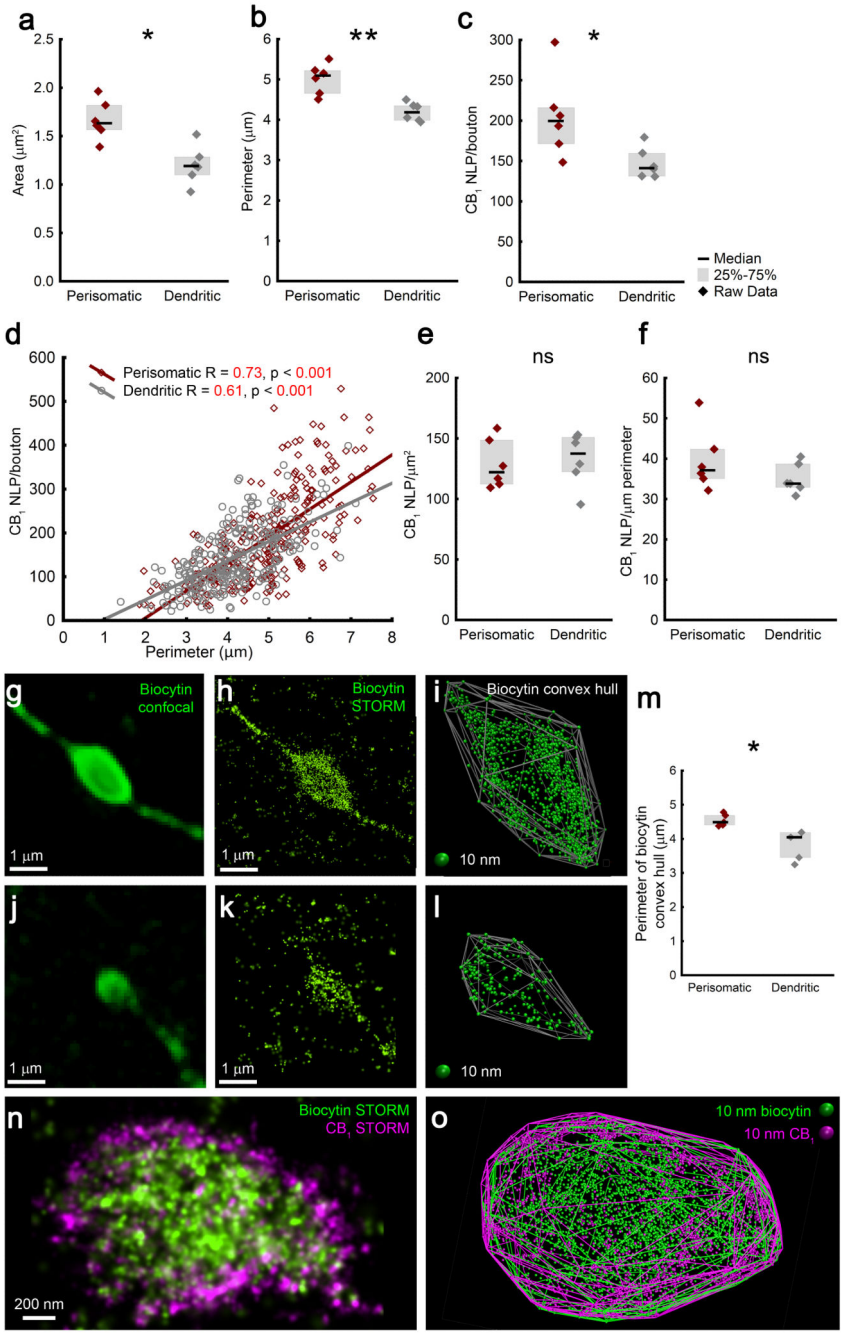

Figure 3. Perisomatic boutons are larger and contain proportionally more CB_1 receptors compared to dendritic boutons

(**a,b**) Perisomatic interneuron terminals are larger than boutons of dendritic interneurons (n = 6 cells/cell type, Mann-Whitney U test, p = 0.004, U = 1 for area, p = 0.002, U = 0 for perimeter). (**c**) Perisomatic axon terminals also carry more presynaptic CB_1 receptors (p = 0.015, U = 3). (**d**) CB_1 NLP shows correlation with bouton size in both interneuron types (n = 279 and 334 boutons, Spearman's correlation). (**e,f**) In contrast, the density of CB_1 is similar between the two cell types (Mann-Whitney U test, p = 0.7 and 0.3, U = 15 and 11 for

NLP over area and perimeter, respectively). (**g,j**) Biocytin-filled axon terminals of CB_1-positive perisomatic (in **g)** and dendritic (in **j)** interneurons labeled by a mixture of Alexa488- and Alexa647-conjugated streptavidin were imaged in confocal (**g,j**) and STORM (**h,k**) modes. (**i,l**) A 3D-convex hull was fitted on the localization points to visualize the surface of axon terminals. (**m**) In agreement with the size difference of CB_1 2D-convex hulls (**b**), the perimeter of biocytin 2D-convex hulls of perisomatic boutons is significantly larger (n = 5 cells/cell type, Mann-Whitney U test, p = 0.012, U = 0). (**n**) Dual-channel directSTORM imaging of an interneuron bouton labeled by Alexa488-conjugated streptavidin, and immunostained against CB_1 using Alexa647. (**o**) Fitting 3D-convex hulls on the biocytin or on the CB_1 localization points results in strikingly similar contours of the structure. Representative images are shown from experiments repeated successfully on two biocytin-filled perisomatic interneurons. Graphs show raw data and median±IQR.

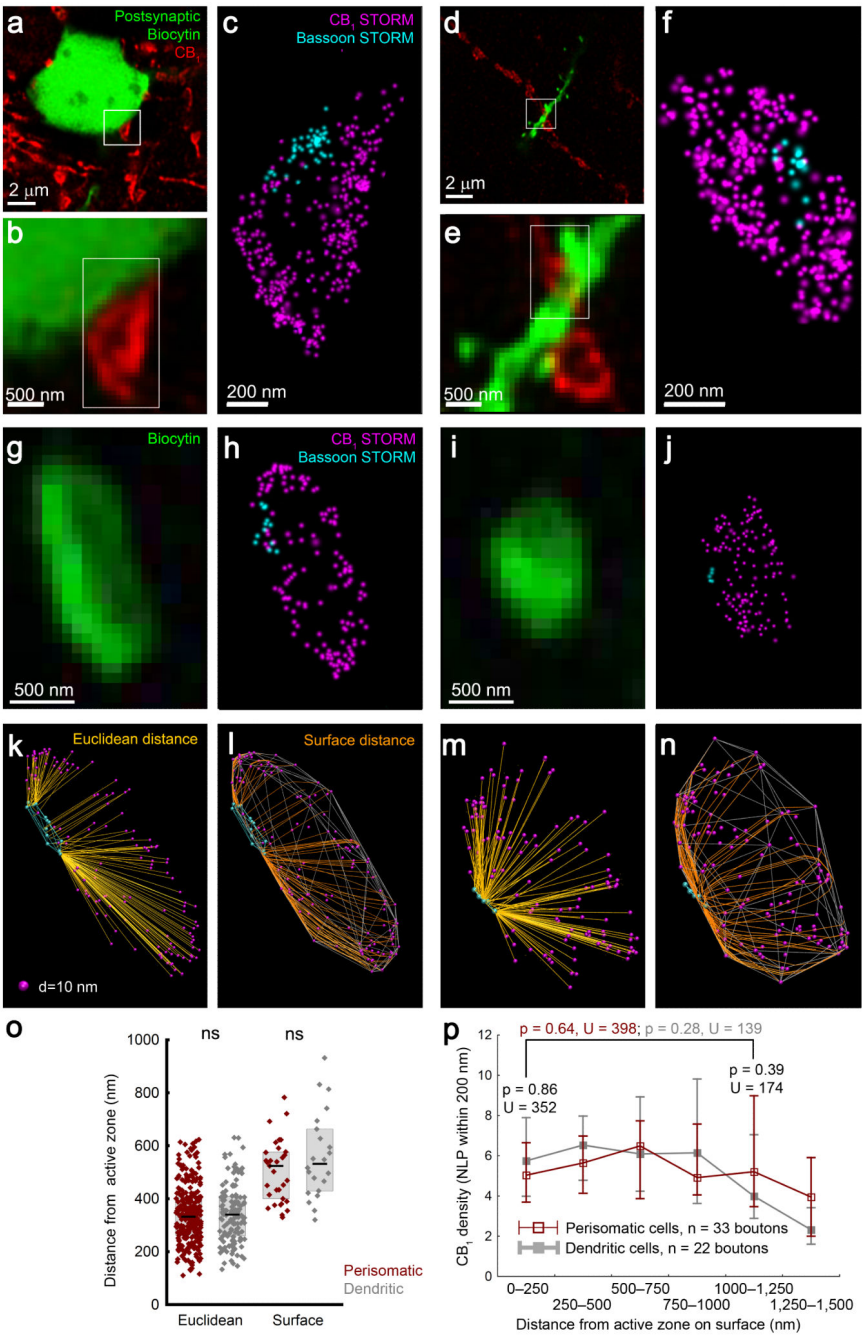

Figure 4. Cell-type-specific multicolor STORM imaging illuminates homogeneous nanoscale distribution of CB_1 receptors on GABAergic axon terminals

(**a,d**) Deconvolved confocal images show a biocytin-filled CA1 pyramidal neuron and adjacent CB_1-positive boutons. (**b,e**) Putative afferents of the labeled neuron are identified. (**c,f**) Dual-channel 3D-STORM demonstrates accumulation of the active zone protein bassoon at the contact site, indicative of a perisomatic and dendritic afferent synapses. Representative images are shown from experiments repeated on 10 biocytin-filled pyramidal neurons. (**g,i**) Confocal images of axon terminals of biocytin-filled perisomatic and dendritic

interneurons, respectively. (**h,j**) Dual-channel 3D-STORM reveals the nanoscale bassoon and CB_1 distribution. (**k,m**) Localization points are visualized in 3D. The Euclidean distances between CB_1 and bassoon LPs can be readily calculated. (**l,n**) To allow intermolecular distance measurements along the structure surface, the shortest paths between CB_1 and bassoon LPs on the bouton surface were determined after fitting a 3D-convex hull on the CB_1 localization points. (**o**) Neither the Euclidean nor the surface distance is different between axon terminals of perisomatic and dendritic interneurons (n = 311 and 141 boutons, Mann-Whitney U test, p = 0.69, U = 21420 for Euclidean distance; n = 33 and 22 boutons, p = 0.31, U = 305 for surface distance). Graphs show raw data and median±IQR. (**p**) The density of receptors (CB_1 NLP within 200 nm from random points of the surface, median ±IQR) is plotted against surface distance from bassoon. Perisynaptic (within 250 nm) and extrasynaptic (1000-1250 nm) CB_1 densities are similar within boutons, and between cell types.

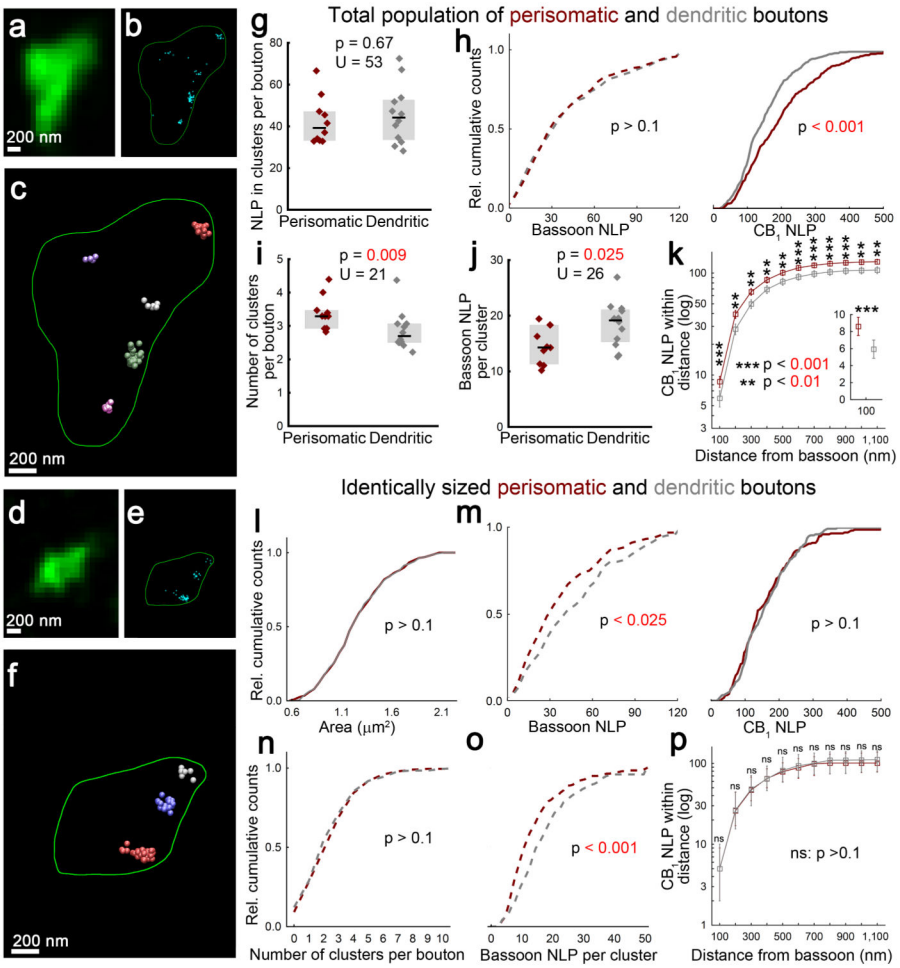

Figure 5. Cell-type-specific and size-independent active zone architecture of GABAergic interneurons

(**a**,**d**) Deconvolved confocal images of boutons of perisomatic and dendritic interneurons. (**b,e**) 3D-STORM images of bassoon-immunostaining within identified axon terminals. (**c,f**) Density-based clustering (DBSCAN) reveals individual bassoon clusters (highlighted in different colors). (**g**) Boutons of perisomatic and dendritic interneurons contain similar NLP (n = 349 and 374 boutons from 10 perisomatic and 12 dendritic cells, respectively, Mann-Whitney U test). (**h**) In contrast to the comparable bassoon NLP (Kolmogorov-Smirnov test), perisomatic boutons contain more CB_1 LPs (n = 279 and 334 boutons from 6 and 6 cells, Kolmogorov-Smirnov test), as determined from separate single staining experiments. (**i**) Axon terminals of perisomatic interneurons contain more bassoon clusters (Mann-Whitney U test), while NLP within individual clusters is lower (**j**). Graphs show raw data and median±IQR. (**k**) Dual-channel STORM imaging demonstrates that CB_1 NLP within any given distance from bassoon labeling is higher in axon terminals of perisomatic interneurons (n = 80–80 randomly selected boutons, Kolmogorov-Smirnov test, plot shows median±IQR). (**l**) To analyze molecular properties independently of bouton size, subsamples of boutons comprising an identical size distribution were selected at random (n = 200-200 boutons, Kolmogorov-Smirnov test). (**m**) In these subsamples, perisomatic axon terminals

contain less bassoon, but similar number of CB_1. (**n**) While the number of bassoon clusters was similar, clusters in boutons of perisomatic interneurons had less NLP (**o**). (**p**) CB_1 NLP within any given distance from bassoon clusters was similar in identically sized subsamples of boutons of the two interneuron types (n = 80-80 boutons, Kolmogorov-Smirnov test).

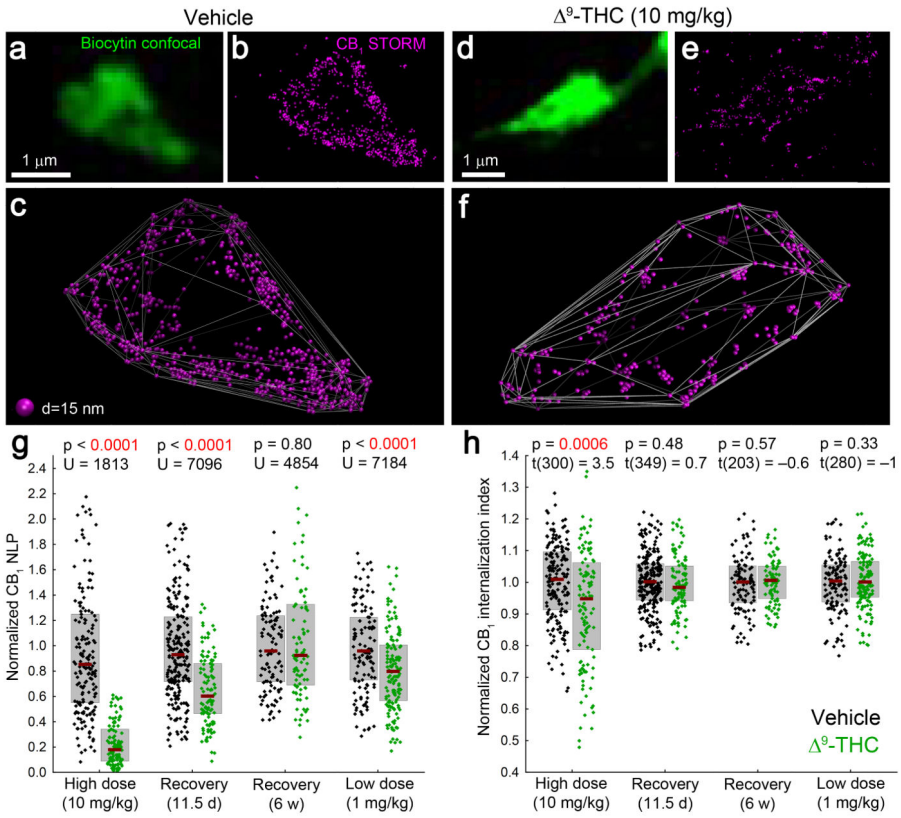

Figure 6. Chronic THC treatment induces long-lasting loss of CB_1 from the plasma membrane of GABAergic axon terminals in a dose-dependent manner

(**a**,**d**) Deconvolved confocal images of axon terminals of perisomatic interneurons, recorded in slices prepared from mice treated with vehicle or THC (i.p. injections twice a day for 6.5 days). (**b,e**) STORM imaging reveals a dramatic THC-evoked reduction of CB_1 localization points. A CB_1 antibody with improved sensitivity derived from transgenic rabbits (Online Methods) was used to enable reliable visualization of CB_1 receptors at low and high levels alike. (**c,f**) Visualization of CB_1 localization points in 3D demonstrates an increased intraterminal accumulation of CB_1 in THC-treated animals. (**g**) Upon chronic administration of 10 mg/kg THC, CB_1 NLP are reduced by 74% (n = 185 and 117 axon terminals from 3 vehicle- and 2 THC-treated animals, Mann-Whitney U test). After a drug-free period of 11.5 days, 53% of CB_1 receptors recovered, but the reduction in NLP (35%) was still significant (n = 283 and 113 boutons from 3 and 3 animals). A longer recovery period of six weeks, however, allowed complete rescue (n = 113 and 92 boutons from 2 and 3 animals). Chronic treatment with a lower (1 mg/kg) dose resulted in a slight (16%) decrease in NLP (n = 129 and 153 boutons from 2 and 3 animals). (**h**) The remaining CB_1 localization points are shifted towards the center of the axon terminal after high dose of THC (unpaired two-sided t-test). However, internalization was not detectable after recovery for 11.5 days or 6 weeks, or after low dose of THC. Graphs show raw data and median±IQR.